

Water Resources Research®

RESEARCH ARTICLE

10.1029/2023WR035251

Key Points:

- Integrating characterization of atmospheric profiles on unmanned aerial vehicle platforms with thermal imagery enables independent plant water use observations
- The ability to capture atmospheric profiles of heat and humidity enables a theoretical approach that minimizes uncertainty in Evapotranspiration estimates
- Atmospheric profile approaches have the potential to substantially improve observations of individual plant water use

Supporting Information:

Supporting Information may be found in the online version of this article.

Correspondence to:

B. E. Morgan,
brynmorgan@ucsb.edu

Citation:

Morgan, B. E., & Caylor, K. K. (2023). Estimating fine-scale transpiration from UAV-derived thermal imagery and atmospheric profiles. *Water Resources Research*, 59, e2023WR035251. <https://doi.org/10.1029/2023WR035251>

Received 3 MAY 2023
Accepted 17 OCT 2023

Author Contributions:

Conceptualization: Bryn E. Morgan, Kelly K. Caylor
Data curation: Bryn E. Morgan
Formal analysis: Bryn E. Morgan
Funding acquisition: Bryn E. Morgan, Kelly K. Caylor
Investigation: Bryn E. Morgan
Methodology: Bryn E. Morgan
Software: Bryn E. Morgan
Visualization: Bryn E. Morgan
Writing – original draft: Bryn E. Morgan

© 2023 The Authors.

This is an open access article under the terms of the [Creative Commons Attribution-NonCommercial License](#), which permits use, distribution and reproduction in any medium, provided the original work is properly cited and is not used for commercial purposes.

Estimating Fine-Scale Transpiration From UAV-Derived Thermal Imagery and Atmospheric Profiles



Bryn E. Morgan^{1,2}  and Kelly K. Caylor^{1,2,3}

¹Department of Geography, University of California, Santa Barbara, Santa Barbara, CA, USA, ²Earth Research Institute, University of California, Santa Barbara, Santa Barbara, CA, USA, ³Bren School of Environmental Science and Management, University of California, Santa Barbara, Santa Barbara, CA, USA

Abstract Accurate and timely observations of individual-scale transpiration are critical for predicting ecosystem responses to climate change. Existing remote sensing methods for measuring transpiration lack the spatial resolution needed to resolve individual plants, and their sources of uncertainty are not well-constrained. We present two novel approaches for independently quantifying fine-scale transpiration using thermal imagery and a suite of environmental sensors mounted on an unmanned aerial vehicle (UAV) platform. The first is a surface energy balance (SEB) approach designed for fine-scale thermal imagery; the second uses profiles of air temperature (T_a) and humidity (h_r) to calculate transpiration from the Bowen Ratio. Both approaches derive the energy equivalent of transpiration, latent heat flux (λE), solely using data acquired from the UAV. We compare the two approaches and their sources of uncertainty using data from several flights at a grassland eddy covariance site in 2021 and 2022 and using typical diurnal conditions to evaluate the uncertainty of λE estimates for each approach. The SEB approach generated independent, UAV-based estimates of λE within ~20% of eddy covariance measurements and was most sensitive to surface temperature and resistance to heat transfer. λE calculated from the Bowen Ratio approach was ~30% higher than tower values due to inaccuracies in T_a and h_r , the main sources of uncertainty in this approach. The Bowen Ratio approach has a lower overall potential uncertainty, indicating its potential for improvement over the SEB approach. Our results are the first physically-based observations of transpiration derived solely from a UAV platform, with no ancillary data inputs.

1. Introduction

Evapotranspiration (ET), the combined processes of evaporation of water from the soil and transpiration of water by plants, is the largest loss term in the terrestrial water balance and plays a key role in the water, carbon, and energy cycles (Oki & Kanae, 2006). Transpiration, or plant water use, accounts for the majority of ET in terrestrial ecosystems (Good et al., 2015; Schlesinger & Jasechko, 2014) and is directly linked to ecosystem productivity through stomatal conductance. Plant transpiration is an important indicator of water stress (Bassiouni & Vico, 2021), and ecosystem responses to hydroclimatic stress are controlled by how individual plants regulate their growth and water status (Anderegg et al., 2018; Konings et al., 2017; McDowell et al., 2008; Roman et al., 2015). Plant water use and responses to stress vary at fine spatial and temporal scales (Anderegg, 2015; Matheny et al., 2014; Z. Zhang et al., 2014), and this heterogeneity in responses is a major source of uncertainty in biosphere-atmosphere feedbacks (Green et al., 2019; Reichstein et al., 2013; Trugman et al., 2018) and predictions of future water, carbon, and energy budgets. Accurate and timely measurements of individual plant transpiration are therefore critical for understanding ecosystem responses to climate change and managing water resources.

With recent advancements in near-surface remote sensing technology, unmanned aerial vehicles (UAVs) have the potential to provide unprecedentedly high spatial and temporal resolution observations of plant water use (McCabe et al., 2017). Transpiration is directly related to vegetation surface temperature (T_s [K]), which makes it possible to derive transpiration from thermal infrared (TIR) imagery. While spatial resolution of thermal imagery from satellites is very coarse (≥ 70 m per pixel), small, lightweight thermal sensors mounted on UAVs can provide centimeter-scale resolution of surface temperature and other variables over hundreds of hectares (Berni et al., 2009; McCabe et al., 2017). As a result, vegetated surfaces—and individual plants—can be isolated from the surrounding landscape, and T_s can be used to calculate transpiration directly, rather than ET. In addition, UAV data can be acquired at high temporal frequencies and during overcast conditions to understand and monitor

Writing – review & editing: Bryn E. Morgan, Kelly K. Caylor

changes in plant physiology and surface-atmosphere mass and energy fluxes under varying radiative, climatic, and hydrological conditions (Vivoni et al., 2014; S. Wang et al., 2020; Simpson et al., 2022). Recently, UAVs have been used to estimate and map ET and its components in a variety of landscapes, including forests (e.g., Marzahn et al., 2020), semi-arid savannas (e.g., Simpson et al., 2022), grasslands (e.g., Brenner et al., 2017, 2018), and agricultural fields and vineyards (e.g., Hoffmann et al., 2016; Kustas et al., 2019; Mokhtari et al., 2021; Nieto et al., 2019; Park et al., 2021). To date, however, UAV-based studies have relied on ground measurements for meteorological data and algorithms designed for coarse-resolution satellite imagery to estimate ET. These two constraints have limited the potential of such platforms to provide independent, fine-scale (sub-meter scale) observations of transpiration over large spatial extents. In addition, sources of uncertainty in flux estimates derived from existing algorithms are not well-constrained, requiring ongoing validation with ground-based ET measurements and obfuscating interpretation of their performance. Improving fine-scale plant water use estimates requires observational platforms that are independent of additional data sources, algorithms designed for their high spatial and temporal resolution data sets, and a robust understanding of the uncertainty in the derived ET observations.

From an observational perspective, operational, transferable approaches for quantifying individual plant water use should be independent of ground-based observations. Physically based remote sensing algorithms require meteorological data, including air temperature (T_a [K]), wind speed (u , [m s^{-1}]), relative humidity (h_r , [%]), and solar radiation, in order to calculate the energy equivalent of ET, latent heat flux (λE [W m^{-2}]) from T_s from surface energy balance (SEB) (K. Zhang et al., 2016; Kalma et al., 2008). In satellite applications, these parameters are typically retrieved from distant weather stations, models, or reanalysis products, which can differ substantially from local conditions (Chen & Liu, 2020; Norman et al., 2000). UAV-based ET studies have primarily used meteorological data from collocated flux towers as inputs to SEB algorithms (e.g., Brenner et al., 2018; Simpson et al., 2022; S. Wang et al., 2019), which has limited the application of UAVs for ET estimation to sites with existing ground instrumentation. Given their versatility as a platform, however, UAVs can be equipped with miniaturized, low-power sensors to measure T_a , h_r , u , and other variables and are increasingly being used to study atmospheric characteristics (Barbieri et al., 2019; Reineman et al., 2013). Such observations have yet to be acquired simultaneously with thermal imagery. Combining very high resolution thermal imagery with high frequency meteorological data on a UAV platform, however, would enable completely independent observations of plant water use.

With the fine-scale thermal and meteorological measurements comes the need for new algorithms designed for the unique spatial scale of UAV-based observations. To date, UAV-based studies of ET have exclusively applied existing remote sensing algorithms to very high resolution thermal imagery to estimate water and energy fluxes. Designed for coarse-resolution satellite thermal imagery, these algorithms assume that pixels are composed of a mixture of vegetation and bare soil and employ a variety of techniques for separating canopy and soil components, including identifying hot and cold endmembers (e.g., Allen et al., 2007; Bastiaanssen, Menenti, et al., 1998; Bastiaanssen, Pelgrum, et al., 1998), constraining ET based on potential ET (e.g., Cleugh et al., 2007; Fisher et al., 2008; Mu et al., 2007), and formulating corrections for aerodynamic terms separately for each component (e.g., Kustas & Norman, 1999; Norman et al., 1995). While satellite algorithms have been used successfully in UAV studies, these approaches are not particularly well-suited for UAV applications, as the resolution is much higher, and each pixel typically comprises a single source. In fact, fine-scale TIR imagery acquired from UAVs often has to be downsampled to generate coarser resolution mixed pixels in order for existing satellite algorithms to be applied (Brenner et al., 2018; Nieto et al., 2019), which undermines the value of such high-resolution data sets. To overcome these challenges, new approaches must be developed specifically for fine-resolution thermal imagery acquired from UAVs (Brenner et al., 2018; Chen & Liu, 2020; Simpson et al., 2022).

Capitalizing on the expanded methodological opportunities enabled by UAV platforms requires robust assessments of the accuracy and uncertainty in both measurements and algorithms used to calculate ET. The accuracy of ET estimates derived from remote sensing algorithms depends on errors in input data, model assumptions, and uncertainties in ground-based validation measurements. While there have been a number of studies comparing various remote sensing algorithms (e.g., García-Santos et al., 2022; Jiménez et al., 2011; Jung et al., 2011; Mueller et al., 2011, 2013; Vinukollu et al., 2011), few identify the sources or spatiotemporal distribution of uncertainty in ET observations (K. Zhang et al., 2016). Nonetheless, the most commonly attributed sources of uncertainty in SEB algorithms are errors in T_s (Cleugh et al., 2007; García-Santos et al., 2022, 2019; K. Zhang et al., 2016) and in the formulation of aerodynamic terms, including aerodynamic resistance (r_{aH} [s m^{-1}])

and temperature (T_{aero} [K]) (Glenn et al., 2007; Kustas et al., 2016; Mallick et al., 2016; Norman et al., 1995; Trebs et al., 2021). Despite numerous new formulations and model updates targeting these issues, discrepancies between ET derived from thermal remote sensing imagery and ground measurements of ET have not improved over the last 50 years (García-Santos et al., 2022). UAV-based approaches have the potential to overcome these challenges by directly characterizing atmospheric profiles of wind, heat, and moisture (Hemingway et al., 2017; Jacob et al., 2018). However, the uncertainty in both observational data inputs and algorithm structure must be adequately examined. A thorough, independent analysis of the sources of uncertainty in water flux estimates is crucial for identifying the optimal approaches under various conditions and improving plant water use estimates (Miralles et al., 2016; K. Zhang et al., 2016).

The goal of this study is to develop a framework for quantifying fine-scale plant water use solely from UAV-acquired data and independently evaluating the sources of uncertainty in remotely sensed estimates of transpiration. The objectives are to: (a) design and implement an observational platform for independent measurements of T_s and meteorological variables; (b) develop physically based algorithms for calculating λE from these independent, fine-scale measurements; and (c) evaluate the sources of uncertainty in these novel algorithms. We present two novel approaches for quantifying fine-scale transpiration solely from UAV-acquired data: one using the SEB equation and one that uses the near-surface atmospheric profiles of heat and moisture to determine λE from the Bowen Ratio. In the first approach, λE is calculated as the residual of the SEB equation, as in existing algorithms. We use a single resistance pathway from the canopy to the atmosphere and evaluate three formulations of r_{ah} . The second approach uses vertical profiles of temperature and humidity to calculate λE from direct measurements of atmospheric conditions, requiring no resistance terms. The sub-meter scale resolution of the thermal imagery allows for extraction of vegetation from the surrounding landscape, so λE can be entirely attributed to transpiration. Using thermal imagery and a suite of environmental sensors mounted on a UAV platform to measure atmospheric conditions, including wind speed, air temperature, and relative humidity, we compare the two approaches and their sources of uncertainty across several flights at a Mediterranean grassland eddy covariance site in Southern California. Finally, we compare the sensitivity of and uncertainty in λE estimates from the two approaches under typical diurnal conditions.

2. Theory

First, we provide an overview of the two approaches. Both use the SEB equation (Equation 1) to derive λE from UAV-acquired data, but the second approach also utilizes the Bowen Ratio (β [-]) to circumvent the need for resistance terms. A summary of the input variables and their sources can be found in Table 1.

2.1. Surface Energy Balance Approach

In the SEB approach, λE is calculated as the residual of the SEB equation; that is,

$$\lambda E = Q_{\text{av}} - H, \quad (1)$$

where Q_{av} is available energy [W m^{-2}]. For most surfaces, $Q_{\text{av}} = R_n - G$, where R_n is net radiation [W m^{-2}] and G is soil heat flux [W m^{-2}]. For vegetation canopies, $G = 0$, so $Q_{\text{av}} = R_n$ and Equation 1 reduces to the canopy energy balance: $\lambda E = R_n - H$, where λE is associated with transpiration only.

While sub-meter resolution T_s data allows for isolation of vegetation from non-vegetated portions of the landscape, G in grasslands is non-negligible. Thus, for the purposes of comparison between our approach and flux tower data, we calculate G during each flight according to Santanello and Friedl (2003), where G is a diurnally varying fraction of R_n :

$$G = R_n \cdot A \cos\left(2\pi \frac{t + c}{B}\right) \quad (2)$$

where A is the amplitude of the diurnal variation in G/R_n [W m^{-2}], B is the period of the variation (24 hr), and c is the phase shift of the curve relative to noon [hr]. These parameters can be derived from the literature or empirical data. Details for how we derived the parameters for Equation 2 are given in Section 3.2.

Net radiation is the sum of incoming and outgoing shortwave and longwave components; that is

Table 1

Input Parameters for Surface Energy Balance (SEB) and Bowen Ratio Algorithms

Type	Description	Variable	Unit	Source or value	Reported measurement accuracy
Atmospheric	Air temperature	T_a	K	UAV (TSM)	± 2 K
	Relative humidity	h_r	%	UAV (TSM)	$\pm 3\%$
	Air pressure	p_a	kPa	UAV (TSM)	± 1 kPa
	Wind speed	u	$m s^{-1}$	UAV (TSM)	$\pm 0.2 m s^{-1}$ ($0-10 m s^{-1}$), $\pm 2\%$ ($11-30 m s^{-1}$)
	Height	z	m	UAV (flight log)	
Surface	Brightness temperature	T_b	K	UAV (Altum)	± 5 K
	NDVI	NDVI	—	UAV (Altum)	
	Vegetation height	h	m	0.3	
	Characteristic leaf dimension ^a	w_l	m	0.01	
	Ratio of horizontal to vertical projected leaf area ^a	x_{LAD}	$m m^{-1}$	1	
	Ratio of z_{0m} to z_{0h} ^a	b	—	10	
	Solar zenith angle ^a	θ_{sun}	radians	UAV (flight log)	
Radiation	Incoming shortwave radiation	$R_{\text{SW}}^{\downarrow}$	$W m^{-2}$	UAV (LI-200R)	$\pm 3\%$

Note. Details on the source and measurement accuracy of each variable can be found in Section 3.

^aOnly required for SEB algorithm.

$$R_n = (1 - \alpha)R_{\text{SW}}^{\downarrow} + R_{\text{LW}}^{\downarrow} - R_{\text{LW}}^{\uparrow}, \quad (3)$$

where α is surface albedo [—], $R_{\text{SW}}^{\downarrow}$ is incoming shortwave radiation [$W m^{-2}$], $R_{\text{LW}}^{\downarrow}$ is incoming longwave radiation [$W m^{-2}$], and R_{LW}^{\uparrow} outgoing longwave radiation [$W m^{-2}$]. Incoming shortwave radiation is measured directly on the UAV, while longwave components are derived from the Stefan-Boltzmann law:

$$R_{\text{LW}}^{\downarrow} = \varepsilon_a \sigma T_a^4 \cdot \varepsilon_s \quad (4)$$

$$R_{\text{LW}}^{\uparrow} = \varepsilon_s \sigma T_s^4, \quad (5)$$

where T_a and T_s are the air and surface temperatures [K], respectively, σ is the Stefan-Boltzmann constant ($5.67 \times 10^{-8} W m^{-2} K^{-4}$), ε_a is atmospheric emissivity [—], and ε_s is the surface emissivity [—]. Incoming longwave radiation is multiplied by ε_s to account for the small amount of longwave radiation that is reflected by the surface. Both ε_s and α are surface properties that can be derived from spectral indices of reflectance; we use the normalized difference vegetation index (NDVI) to calculate ε_s and α according to Gao (1995) and Van de Griend and Owe (1993), respectively. Atmospheric emissivity depends on T_a and vapor pressure (e_a [kPa]), which is itself a function of T_a and relative humidity (h_r [%]) (Buck, 1981), and is calculated according to Brutsaert's equation for clear skies (Brutsaert, 1975).

Sensible heat flux is given by the flux-gradient relationship for heat:

$$H = \rho_a c_p \frac{\theta_s - \theta_a}{r_H}, \quad (6)$$

where ρ_a is the density of air [$kg m^{-3}$], c_p is the heat capacity of air at constant pressure [$J kg^{-1} K^{-1}$], θ_s and θ_a are the potential temperatures of the surface and the air [K], respectively, and r_H is the total resistance to heat transfer [$s m^{-1}$]. Potential temperatures are used in place of T_s and T_a to account for differences in air pressure (p_a [kPa]) between measurement heights. Here, we standardize T_a to the surface, so $\theta_s = T_s$, and $\theta_a = T_a + (z - z_0)\Gamma$, where Γ is the adiabatic lapse rate, approximated to the rate for dry air ($9.75 \times 10^{-3} K m^{-1}$) (Bonan, 2016).

The resistance to heat transfer between the surface and some height z [m] in the atmospheric boundary layer r_H can be written

$$r_H = r_{aH} + r_{bH}, \quad (7)$$

where r_{aH} is the aerodynamic resistance [s m^{-1}] and r_{bH} is the bulk surface (i.e., leaf or canopy) boundary layer resistance [s m^{-1}]. This so-called boundary layer resistance represents the resistance to heat transfer along the path between the surface, with temperature T_s , and the air just above the surface that is freely exchanged with the atmosphere via convection (H) with temperature T_{aero} [K]. The boundary layer resistance is given by the equation (McNaughton & Van Den Hurk, 1995):

$$r_{bH} = \frac{c'}{LAI} \left(\frac{w_l}{u(d_0 + z_{0m})} \right)^{1/2}, \quad (8)$$

where $c' = 90 \text{ m s}^{-1}$ is a weighting coefficient (Grace, 1981), LAI is the leaf area index [-], w_l is the characteristic leaf dimension [m], and $u(d_0 + z_{0m})$ is the wind speed at the source height for momentum transfer, defined as the sum of the zero-plane displacement height (d_0 [m]) and the roughness length for momentum (z_{0m} [m]) (see Supporting Information S1 for how these are calculated).

According to Monin-Obukhov Similarity Theory (Monin & Obukhov, 1954), the bulk aerodynamic resistance between the effective surface, defined as the source for heat transfer with height $z_{0h} + d_0$ and temperature T_{aero} , and some height z in the mixing layer with air temperature T_a is:

$$r_{aH} = \rho_a c_p \frac{\theta_{\text{aero}} - \theta_a}{H} = \frac{\left[\ln\left(\frac{z-d_0}{z_{0m}}\right) - \Psi_m\left(\frac{z-d_0}{L}\right) + \Psi_m\left(\frac{z_{0m}}{L}\right) \right] \left[\ln\left(\frac{z-d_0}{z_{0h}}\right) - \Psi_h\left(\frac{z-d_0}{L}\right) + \Psi_h\left(\frac{z_{0h}}{L}\right) \right]}{\kappa^2 u}, \quad (9)$$

where u is the wind speed at height z , $\kappa = 0.41$ is the von Kármán constant [-], z_{0h} is the roughness length for heat transfer [m], L is the Monin-Obukhov length [m], and Ψ_m and Ψ_h are correction functions to account for the effects of atmospheric stability on momentum and heat transport, respectively. The inclusion of the boundary layer resistance term in Equation 7 allows us to use θ_s in Equation 6 rather than θ_{aero} .

Although the stability functions (Ψ_m and Ψ_h) have been studied extensively, data show substantial variability compared to predictions from various empirical formulations (Hogstrom, 1996). Furthermore, Ψ_m and Ψ_h depend on Monin-Obukhov length L [m], which in turn depends on both friction velocity (u_* [m s^{-1}]) and the turbulent fluxes, H and λE , themselves (Obukhov, 1971). Thus, Equation 9 cannot be solved directly and must be determined iteratively.

The difficulty of characterizing atmospheric stability makes r_{aH} a major source of uncertainty in SEB approaches. To evaluate their influence on H and λE , we compare three methods for estimating r_{aH} : one that assumes neutral conditions and two different formulations of the stability terms—one simple (Dyer, 1974; Dyer & Hicks, 1970, “Dyer”) and one more complex (Brutsaert, 1992, 1999; Cheng & Brutsaert, 2005, “Brutsaert”). The neutral case eliminates the need for the stability terms, as L is infinite and $\Psi_M = \Psi_H = 0$, so Equation 9 can be solved based on wind speed alone. However, because the atmosphere is rarely neutral during the daytime, the non-neutral cases provide a more realistic representation of actual conditions. We compare the original stability functions (Dyer, 1974; Dyer & Hicks, 1970) to the more complex, but commonly used formulations (Brutsaert, 1992, 1999; Cheng & Brutsaert, 2005). In both cases, Equations 7–9 are solved iteratively, starting from neutral conditions ($L = \infty$) to calculate initial fluxes, and continuing until the difference between successive solutions for L is below some minimal threshold (0.001) or a maximum number of iterations has been reached ($n = 15$). In all cases, we use $d_0 = 0.65 \text{ hr}$ (Brutsaert, 1982), $z_{0m} = 0.125 \text{ hr}$ (Norman et al., 1995), and $z_{0h} = 0.1z_{0m}$ (Bonan, 2016).

2.2. Bowen Ratio Approach

Equations 6 and 9 are solutions to the flux-gradient equations for the case when values of u , T_a , and h_r are only known at a single height. However, if at least two of these quantities are known at multiple heights in the near-surface layer, the turbulent fluxes can be directly calculated from the vertical profiles without the need for resistance terms r_{aH} and r_{bH} (Brutsaert, 2005).

The Bowen Ratio approach uses measurements of T_a and h_r at two heights to calculate λE according to the Bowen Ratio, which relates sensible to latent heat flux:

$$\beta = \frac{H}{\lambda E} = \frac{c_p (\theta_{a2} - \theta_{a1})}{\lambda_v (q_2 - q_1)}, \quad (10)$$

where q is specific humidity [kg kg^{-1}], λ_v is the latent heat of vapourization of water [J kg^{-1}], and the subscripts 1 and 2 denote quantities at heights z_1 [m] and z_2 [m] above the surface, respectively. Rearranging Equation 10 and substituting for H in the SEB equation (Equation 1) gives a solution for λE that does not depend on r_H :

$$\lambda E = \frac{Q_{av}}{1 + \beta}. \quad (11)$$

Because remote sensing platforms used for ET estimation typically cannot provide measurements of atmospheric properties, the Bowen Ratio has never been used to derive spatially distributed flux observations from thermal imagery. UAV-mounted sensors can rapidly and repeatedly sample the atmosphere at multiple heights near the surface, however, so Equation 10 can be solved. Combining β with fine-scale observations of net radiation, calculated from T_s and other variables (Equations 3–5), provides a way to calculate λE from physical principles without introducing empirically derived stability functions (Equation 11).

3. Methods

3.1. Data Collection

3.1.1. Study Area and Instrumentation

To test and validate the approaches, flights were conducted at an eddy covariance site ($34.52548^\circ\text{N}, 120.41542^\circ\text{E}$) at the Jack and Laura Dangermond Preserve, located on the central coast of California, USA. The study site is a 40-ha Mediterranean grassland with an average vegetation height of approximately 0.3 m during the flight campaigns. The region is characterized by a Mediterranean climate, with warm, dry summers and a cool, winter wet season (November to April; Butterfield et al., 2019). Mean annual precipitation is between 300 and 450 mm (Santa Barbara County Flood Control District, 2022).

The eddy covariance instrumentation includes a three-dimensional (3-D) sonic anemometer (Gill WindMaster, Gill Instruments Limited, Hampshire, UK) and an open-path infrared gas analyzer (LI-7500DS, LI-COR Biosciences, Lincoln, NE, USA) for high-frequency flux measurements at a height of 3.8-m. Raw eddy covariance data are collected at 10 Hz and fluxes are calculated in 30-min intervals using EddyPro software (LI-COR Biosciences, Lincoln, NE, USA). In addition to the flux instruments, the tower is equipped with a 4-channel net radiometer (CNR4, Kipp & Zonen, Delft, The Netherlands) and a temperature and humidity probe (HMP155, Vaisala, Vantaa, Finland) also mounted at 3.8 m, as well as three soil heat flux plates (HFP01SC, Hukseflux, Delft, The Netherlands) and a rain gauge (TR-525M, Texas Electronics, Dallas, TX, USA). Soil moisture probes (HydraProbe, Stevens Water, Portland, OR, USA) are installed at depths of 6.35 and 23 cm to provide continuous measurements of soil water content.

3.1.2. UAV System and Instrumentation

The UAV platform consists of a DJI Matrice 600 Pro (M600 Pro) hexacopter UAV equipped with a suite of environmental sensors (Figure 1). The M600 Pro is a professional-grade UAV with a 5.5-kg maximum payload, allowing simultaneous measurements from multiple onboard sensors to be obtained during a single flight. Imagery is acquired using a dual multispectral and TIR sensor (MicaSense Altum, MicaSense Solutions, Seattle, WA, USA). The Altum provides six radiometrically calibrated bands—five in the visible to shortwave infrared (VSWIR) wavelength range (blue, green, red, red-edge, near-infrared) and one TIR—with an image resolution of $2,064 \times 1,544$ in the VSWIR and 160×120 in the TIR bands. A separate Downwelling Light Sensor (DLS2, MicaSense Solutions, Seattle, WA, USA) mounted on top of the UAV provides Global Positioning System data for the Altum and calibration information for VSWIR imagery under changing light conditions. A high-precision global navigation satellite system (GNSS) module (Emlid Reach M2, Emlid, Budapest, Hungary) is integrated with the camera, recording location data for each image, to improve the accuracy of image georeferencing.

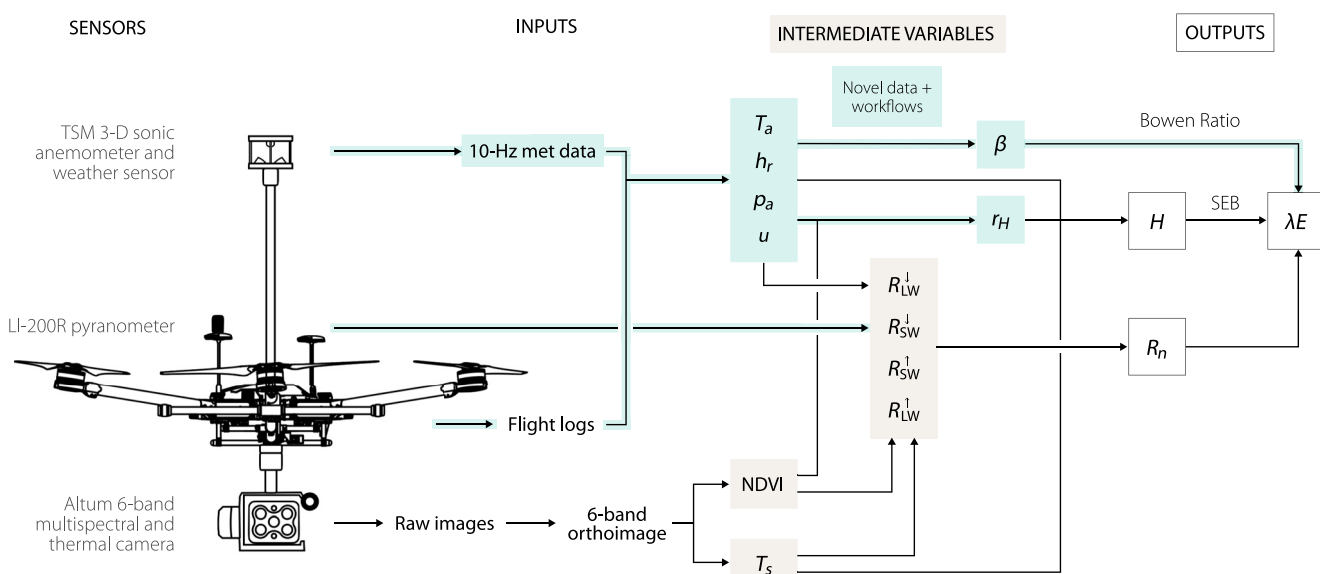


Figure 1. The unmanned aerial vehicle (UAV) system, data inputs, and workflow for the two algorithms. The UAV system (left) includes a 6-band multispectral and thermal camera, two pyranometers, and a 3-D sonic anemometer and weather sensor. Data inputs from each source on the UAV are shown along with the main steps in the processing workflow. Novel data and workflows are highlighted in blue.

In addition to high resolution imagery, the UAV system includes meteorological sensors to measure all additional variables required for solving Equations 1 and 11. Two LI-200R pyranometers (LI-COR Biosciences, Lincoln, NE, USA) are mounted on the UAV to measure incoming and outgoing shortwave radiation, and a lightweight, 3-D ultrasonic anemometer and weather sensor (TriSonica Mini Wind and Weather Sensor, Anemoment, LLC, Longmont, CO, USA; TSM) is installed on a mast mounted on top of the UAV to measure u , T_a , h_r , and p_a .

The TSM mast extends 53.8 cm above the propeller plane—above the manufacturer-recommended minimum height of ~50 cm—to ensure minimal influence of propeller wash on wind vector measurements. Data from the TSM and pyranometers are recorded at a frequency of 5 Hz on an on-board data logger (DL222, Anemoment, LLC, Longmont, CO, USA) and downloaded after each flight.

3.1.3. Flight Campaigns

Flights were conducted in the 2021 and 2022 growing seasons. A total of 50 flights are included in this study consisting of 16 primary flights during which all data were collected and an additional 34 flights during which only meteorological data were collected. Details for the main 16 primary flights are shown in Table 2. The additional 34 flights were conducted between 1 March and 1 April 2021. Data were collected in 1.5–2 hr intervals between 9:00 and 16:00 to compare UAV-derived λE to tower values under various diurnal conditions. Average flight duration was 17 min, and flights were timed such that they roughly fell within a single 30-min averaging period of the eddy covariance data.

Images were collected with 90% overlap and 80% sidelap in the VSWIR bands to facilitate mosaicking. MicaSense calibration panel images were obtained before and after each flight for use in radiometric calibration of the VSWIR images during post-processing. The data logger was powered on approximately 5–10 min before takeoff and recorded data while the UAV was on the ground ($z_1 = 1.5$ m), throughout each flight ($z_2 = 50.5$ or 60.5 m), and for 5–10 min after landing.

Table 2
Unmanned Aerial Vehicle Flight Details

Date	Acquisition time	Flying height (m)	Comments
01 March 2021	12:30–12:48	50	No R_{SW}^I data
24 March 2021	11:58–12:16	60	No R_{SW}^I data
18 January 2022	10:09–10:26	60	
18 January 2022	11:11–11:28	60	
18 January 2022	12:10–12:27	60	
18 January 2022	13:08–13:26	60	
18 January 2022	14:20–14:35	60	
25 January 2022	10:00–10:18	60	
25 January 2022	11:04–11:23	60	
25 January 2022	12:07–12:23	60	
25 January 2022	13:07–13:24	60	
25 January 2022	14:01–14:18	60	No meteorological data
28 January 2022	12:10–12:27	60	
28 January 2022	13:18–13:37	60	
28 January 2022	14:04–14:20	60	
28 January 2022	15:04–15:21	60	

Note. Data collected during the 16 flights shown here included VSWIR and thermal imagery and meteorological data (except where indicated). An additional 34 flights were conducted in 2021 to collect additional meteorological data without imagery.

3.1.4. Processing of UAV Data

Raw images obtained during the flights were processed in Agisoft Metashape Professional (Agisoft, LLC, St. Petersburg, Russia) to generate orthoimages and digital elevation models for each flight using structure-from-motion photogrammetry (Westoby et al., 2012). Image metadata was used for vignetting correction and reconstructing camera locations. The five VSWIR bands were radiometrically calibrated using pre- and post-flight calibration panel images for all flights. Image trigger locations were updated with high-precision GNSS data using the post-processing kinematics method, which uses the position of a base station to perform offset corrections to the position of a rover module. In this case, image trigger locations from the on-board rover module were corrected in Emlid Studio 1.3 using logs from a local base receiver (Reach RS2, Emlid, Budapest, Hungary) set up in the field prior to each campaign. Point clouds were generated for each flight, followed by a digital elevation model and a six-band orthoimage.

Raw log files from the M600 Pro were downloaded following each flight and decoded to generate 10-Hz flight logs that included information about the UAV's position, velocity, and orientation. Meteorological data were filtered and flagged for erroneous values, smoothed using a rolling median filter, and aligned with the flight logs based on their timestamps and the 3-D vectors of wind and aircraft speed. Raw 3-D wind speed components were corrected for the velocity and orientation of the UAV and used to calculate a corrected total wind speed. The vertical component of wind speed was ignored in this calculation as the TSM's design obstructs true vertical wind speed measurements. Because flux calculations assume that the average vertical wind speed over the averaging period is 0 m s⁻¹ (Aubinet et al., 2012), ignoring vertical wind speed should not affect the derived turbulent fluxes.

3.2. Implementation of SEB and Bowen Ratio Approaches

Both the SEB and Bowen Ratio approaches require information about surface characteristics and atmospheric and radiative conditions, as described in Section 2. The input variables and their sources are described in Table 1.

Meteorological data (T_a , h_r , p_a , and u) were averaged at two heights: while the UAV was on the ground ($z_1 = 1.5$ m) and at the flying altitude ($z_2 = z_{\text{UAV}} + 0.54$ m, where z_{UAV} [m] is the height of the aircraft). For one flight, no meteorological data were recorded, so tower values were substituted. As data were only available at one height, the Bowen Ratio approach was not applied to this flight.

NDVI was calculated from the orthoimages and used to derive α , ε_s , and LAI as described in Supporting Information S1. Corrections for atmospheric effects between the surface and the sensor and surface emissivity were applied to convert the raw, radiometric temperature (T_b [K]) to surface temperature following Aubrecht et al. (2016) and (Heinemann et al., 2020) (see Supporting Information S1 for details; Minkina & Dudzik, 2009; Minkina & Klecha, 2015; Tran et al., 2017).

Parameters for the soil heat flux equation (Equation 2) were derived using measurements of R_n and G from the flux tower. To match the conditions of our flights, we used daytime (7:00 to 20:00) measurements from the wet season to determine A and c using a non-linear least squares fit, yielding values of $A = 0.2 \text{ W m}^{-2}$ and $c = -4 \text{ hr}$. We then calculated a landscape-scale average G value for each flight based on the corresponding time of day using Equation 2.

Radiation components were calculated separately and used to calculate R_n . Measurements of $R_{\text{SW}}^{\downarrow}$ from the UAV were averaged for each flight. As the terrain was flat and the homogeneous grass cover minimizes shadow effects, we assumed $R_{\text{SW}}^{\downarrow}$ was the same across the flight area and applied this mean value to the entire image. The additional radiation components— R_{SW}^{\uparrow} (pixelwise), $R_{\text{LW}}^{\downarrow}$ (scalar), and R_{LW}^{\uparrow} (pixelwise)—were calculated according to Equations 3–5 and combined with $R_{\text{SW}}^{\downarrow}$ (scalar) to calculate R_n for each pixel according to Equation 3.

For each flight, we calculated H and λE in four ways: using the SEB approach with each of the three formulations of r_{aH} described in Section 2.1, and using the Bowen Ratio approach. In the SEB approach, a single r_{aH} value is calculated for the flight area based on the mean value of L at the end of each iteration. r_{bH} is calculated on a pixel-wise basis as it varies with LAI.

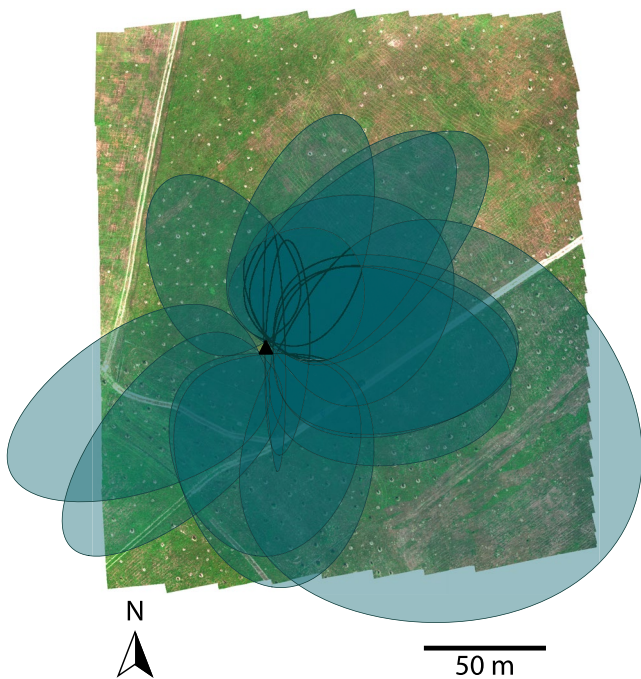


Figure 2. Tower footprints for each of the 16 unmanned aerial vehicle flights. The shaded regions represent 80% of the total fetch area of the tower during each flight. The black triangle denotes the location of the eddy covariance tower (34.52548°N , $120.41542^{\circ}\text{E}$).

spiration to total ET (L. Wang et al., 2014; Wei et al., 2017). Thus, λE from the two sources—the tower and the UAV—should be comparable.

Because eddy covariance provides a single flux measurement over the tower's fetch area, the fine-scale fluxes from the UAV were aggregated to single, landscape-scale values based on the footprint of the tower at the time of each flight. The source area for a tower depends on tower height and surface roughness and varies over time with wind direction and atmospheric stability. We used the Flux Footprint Prediction model (Kljun et al., 2015) to model the two-dimensional density distribution source area based on scaling the crosswind distribution. For each flight, the spatially distributed footprint density was calculated at a resolution of 0.5 m. Source-weighted mean fluxes were calculated by multiplying the fine-scale UAV fluxes by the tower footprint for each flight. The UAV orthoimages covered 86.1% of the tower fetch areas on average, ranging between 75.0% and 96.2% for the 16 flights (Figure 2).

A well-known problem in with the eddy covariance technique is the discrepancy between the sum of turbulent fluxes, $H + \lambda E$, and available energy, $R_n - G$ (Foken, 2008; Mauder et al., 2020). To correct for this discrepancy, we forced closure of the energy balance by attributing the energy balance residual to λE , as this is implicit in the UAV algorithms.

We compared eddy covariance-derived H and λE with the source-weighted mean fluxes for each of the 4 methods (Neutral, Dyer, Brutsaert, and Bowen) by evaluating the RMSD, r^2 , and MD values between the two sets of measurements, as with the input parameters.

3.4. Analytical Uncertainty in λE

In addition to comparing the SEB and Bowen Ratio approaches empirically using the UAV- and eddy covariance-derived fluxes, we evaluated their performance analytically. To do so, following Beven (1979) and Qiu et al. (1998), we developed a framework for estimating the uncertainty and sources of uncertainty in λE derived from each approach based on analytical solutions to the partial derivatives of Equations 1 and 11.

3.3. Comparison of UAV and Eddy Covariance Fluxes

3.3.1. Comparison of UAV- and Tower-Derived Input Parameters

To assess the quality of the UAV-based meteorological measurements, we compared the measured parameters (T_a , h_r , u , p_a) to corresponding tower values. Because the measurement heights were not the same, we scaled the original tower values ($z = 3.8$ m) to the measurement heights of the UAV for each flight ($z_1 = 1.5$ m and $z_2 = 50.5$ or 60.5 m) using turbulent fluxes from the tower to derive atmospheric profiles of wind, heat, and water vapor. This technique is detailed in Supporting Information S1.

We also compared UAV-derived R_n and each of the four radiation components ($R_{\text{SW}}^{\downarrow}$, R_{SW}^{\uparrow} , $R_{\text{LW}}^{\downarrow}$, R_{LW}^{\uparrow}) to the values measured by the tower. Statistics including the root-mean-squared deviation (RMSD), coefficient of determination (r^2), and mean difference (MD) were calculated for each variable and used for assessment.

3.3.2. Turbulent Fluxes

While the approaches are designed to retrieve fine-scale measurements of transpiration, we first evaluated the performance of each approach by comparing the landscape-scale aggregated turbulent fluxes to eddy covariance values, a necessary first step before implementation in locations without additional flux measurements. A limitation with this comparison is that the λE measured by the tower corresponds to total ET, while our algorithms account only for transpiration. However, at our study site—a relatively homogeneous grassland landscape with a single-layer vegetation canopy—we estimate that transpiration comprises 81%–95% of total ET during our growing season flights, based on the relationship between LAI and the ratio of transpiration to total ET (L. Wang et al., 2014; Wei et al., 2017). Thus, λE from the two sources—the tower and the UAV—should be comparable.

3.4.1. Analytical Framework

A general expression for λE as a function of n input variables x can be written

$$\lambda E = f(x_1, x_2, x_3, \dots, x_n). \quad (12)$$

For some change (or uncertainty) in x_i , Δx_i , the resulting λE is expressed as

$$\lambda E + \Delta \lambda E = f(x_1 + \Delta x_1, x_2 + \Delta x_2, x_3 + \Delta x_3, \dots, x_n + \Delta x_n), \quad (13)$$

where $\Delta \lambda E$ is the change in λE resulting from Δx_i . Ignoring second-order and higher terms, the total change in λE , $\Delta \lambda E$, due to the uncertainty in each input variable can be expressed as a Taylor series expansion of Equation 13:

$$\Delta \lambda E = \frac{\partial \lambda E}{\partial x_1} \Delta x_1 + \frac{\partial \lambda E}{\partial x_2} \Delta x_2 + \frac{\partial \lambda E}{\partial x_3} \Delta x_3 + \dots + \frac{\partial \lambda E}{\partial x_n} \Delta x_n, \quad (14)$$

where $\frac{\partial \lambda E}{\partial x_i}$ represents the sensitivity of λE to x_i and $\frac{\partial \lambda E}{\partial x_i} \Delta x_i$ is the uncertainty in λE due to x_i .

The expanded forms of Equations 1 and 11 are given in Supporting Information S1. From these equations, it can be seen that λE is dependent on $R_{\text{SW}}^{\downarrow}$ and T_s , as well as the meteorological input variables, T_a , h_r , and p_a . For the sake of simplicity, we ignore the effects of errors in the albedo and emissivity terms, as well as the dependence of r_H on λE in Equation 9. Thus, the total uncertainty in λE in the SEB approach, $\Delta \lambda E_{\text{SEB}}$ [W m^{-2}], is:

$$\Delta \lambda E_{\text{SEB}} = \frac{\partial \lambda E}{\partial T_s} \Delta T_s + \frac{\partial \lambda E}{\partial r_H} \Delta r_H + \frac{\partial \lambda E}{\partial R_{\text{SW}}^{\downarrow}} \Delta R_{\text{SW}}^{\downarrow} + \frac{\partial \lambda E}{\partial T_a} \Delta T_a + \frac{\partial \lambda E}{\partial h_r} \Delta h_r + \frac{\partial \lambda E}{\partial p_a} \Delta p_a. \quad (15)$$

The total uncertainty in λE calculated from the Bowen Ratio approach, $\Delta \lambda E_{\text{BR}}$ [W m^{-2}], is:

$$\begin{aligned} \Delta \lambda E_{\text{BR}} = & \frac{\partial \lambda E}{\partial T_s} \Delta T_s + \frac{\partial \lambda E}{\partial R_{\text{SW}}^{\downarrow}} \Delta R_{\text{SW}}^{\downarrow} + \frac{\partial \lambda E}{\partial T_{a1}} \Delta T_{a1} + \frac{\partial \lambda E}{\partial T_{a2}} \Delta T_{a2} \\ & + \frac{\partial \lambda E}{\partial h_{r1}} \Delta h_{r1} + \frac{\partial \lambda E}{\partial h_{r2}} \Delta h_{r2} + \frac{\partial \lambda E}{\partial p_{a1}} \Delta p_{a1} + \frac{\partial \lambda E}{\partial p_{a2}} \Delta p_{a2}. \end{aligned} \quad (16)$$

The partial derivatives in Equations 15 and 16 are given in the Supporting Information S1.

3.4.2. Analytical Uncertainty in UAV-Derived λE

We used Equations 15 and 16 to compare the sources of uncertainty in the UAV-derived estimates of λE_{SEB} and λE_{BR} . Differences between tower and UAV values of each parameter during each flight were used for the corresponding uncertainties (Δx_i). For the meteorological variables, uncertainties ΔT_a , Δh_r , and Δp_a were calculated by scaling the tower data as described in Section 3.3.1 and in Supporting Information S1. Surface temperature values for the tower were calculated by inverting Equation 5 using R_{LW}^{\uparrow} measured by the tower's downward-facing pyrgeometer and assuming a surface emissivity of 0.98 (i.e., a vegetated surface). Tower r_H was calculated by inverting Equation 6 with this T_s and measured values of H , T_a , ρ_a , and c_p .

3.4.3. Analysis of Diurnal λE Sensitivity and Uncertainty

To compare the approaches more generally, we evaluated the relative sensitivities and uncertainties of λE_{SEB} and λE_{BR} with respect to each variable under varying diurnal conditions. The relative sensitivity of λE to each variable can be determined by perturbing each variable by an equal percentage of its value. In this case, the fraction of $\Delta \lambda E$ that is due to x_i , that is, $\frac{\partial \lambda E}{\partial x_i} \frac{\Delta x_i}{\Delta \lambda E}$, represents the importance of x_i . On the other hand, if typical measurement uncertainties are used for Δx_i , $\Delta \lambda E$ is an estimate of the total uncertainty in λE , and $\frac{\partial \lambda E}{\partial x_i} \Delta x_i$ is the uncertainty in λE that is due to x_i .

We calculated the relative sensitivities and sources of uncertainty in each approach in half-hourly intervals from early morning to evening (5:30 to 20:00). For each half-hour period, we calculated the median wet-season values of T_s , r_H , $R_{\text{SW}}^{\downarrow}$, T_a , h_r , and p_a from the tower data between January 2021 and November 2022. Tower data were masked during rainfall, and wet season values were selected using a soil moisture threshold of $0.18 \text{ m}^3 \text{ m}^{-3}$, below which ET reduces sharply at the tower site. Equation 16 requires parameter values at two heights. We again scaled the median half-hourly values to 1.5 m (z_1) and 60.5 m (z_2) to align with the approximate measurement heights of the UAV data according to the approach described in Section 3.3.1 and Supporting Information S1.

3.4.4. Analysis of Potential Uncertainty in λE

While the equal percentage and typical measurement errors are useful for comparing the relative importance of each variable, they are less useful for understanding the absolute uncertainty in λE , as Equations 15 and 16 depend strongly on the magnitude of and uncertainty in each variable. To characterize the possible range of uncertainties in λE calculated from each approach, we used a Monte Carlo approach to generate probability distributions of $\Delta\lambda E_{SEB}$ and $\Delta\lambda E_{BR}$. The reported measurement accuracy of each variable x_i was assumed to represent the 95% confidence interval of Δx_i , where Δx_i is normally distributed around 0. In each simulation, uncertainty values were obtained by randomly sampling from each variable's uncertainty distribution (i.e., the distribution of Δx_i) and used to calculate $\frac{\partial \lambda E}{\partial x_i} \Delta x_i$. The distributions of uncertainty due to each variable $\frac{\partial \lambda E}{\partial x_i} \Delta x_i$ derived from 100,000 simulations were summed to generate stacked probability distributions of the total $\Delta\lambda E$, representing the range of possible uncertainties for each approach.

We generated distributions of $\Delta\lambda E$ for each approach using typical morning (9:00–9:30) and midday (13:00–13:30) parameter values for the wet season, as in the previous section. A total of four stacked probability distributions were generated, one for each approach at each time of day.

4. Results

4.1. Input Parameters

Meteorological conditions (T_a , h , p_a , and u) measured on the UAV from all 50 flights are compared with corresponding values generated from the tower data in Figure 3. The UAV values generally showed good agreement with the tower-derived values, particularly in the case of p_a , though a few notable trends emerged. Air temperature from the UAV was 1.5–2°C higher than tower values on average, with a slope of <1. As a result, the UAV values were too high at cool air temperatures and too low at hotter air temperatures. Relative humidity values had a less clear trend, but showed greater scatter under more humid conditions. Measurements of h , while the UAV was on the ground were 1.7% lower than tower profile values, while in-flight values were 5.7% lower, resulting in an overestimation of the humidity gradient for many of the flights. Wind speed measured by the UAV showed no obvious bias, but had more noise than the other variables. Negative u_1 values were predicted for two flights when the actual wind speed was very low (<0.5 m s⁻¹). Notably, UAV wind speeds at both heights were roughly the same in terms of their noise and offset from the tower values; on average, ground and in-flight measurements from the UAV were 0.32 and 0.23 m s⁻¹ higher than the tower, respectively, indicating that the correction for the speed of the UAV during the flight was successful.

The UAV also measured R_{SW}^\downarrow , and the other radiation components were calculated from UAV-based measurements of T_a , T_s , and NDVI. Overall, calculated net radiation was higher than the values from the tower's CNR4 by an average of 34.6 W m⁻² (Figure 4). Most of this discrepancy is due to the disagreement between R_{SW}^\downarrow values from the two pyranometers. The UAV-mounted LI-200R measurements averaged 34.4 W m⁻² higher than the CNR4. Outgoing shortwave radiation (R_{SW}^\uparrow) was underestimated by 19.5 W m⁻², which further contributed to the discrepancy between R_n values. Most of this was made up for by net R_{LW} , which generally showed good agreement, with UAV values slightly lower (12.8 W m⁻²) than tower values.

4.2. Turbulent Fluxes

Figure 5 shows an example of the maps of NDVI, T_s , and λE generated from the orthoimages for each flight. The average spatial resolution of the VSWIR orthoimages was 2.41 cm, and the average spatial resolution of the TIR images was 40.26 cm.

4.2.1. Comparison of λE From Each Approach With Eddy Covariance Measurements

The SEB approach showed better agreement with turbulent fluxes from the tower than the Bowen Ratio approach, but only when atmospheric stability was considered (Figure 6). While the neutral model yielded values comparable to the tower for λE (MD = 11.43 W m⁻²), estimates of H were worse than the other SEB approaches (MD = -46.69 W m⁻²).

The SEB approach with the Brutsaert formulation of r_{aH} showed a slightly better match (H : MD = -8.26 W m⁻²; λE : MD = -26.97 W m⁻²) with the tower data than the Dyer formulation (H : MD = 2.66 W m⁻²; λE : MD = -37.91 W m⁻²), but there was no major difference between the two formulations for either of the fluxes. The Bowen Ratio approach underestimated H by an average of 49.15 W m⁻² and overestimated λE by an average of 44.86 W m⁻². Compared to the SEB approaches, however, there was much more variation in λE between

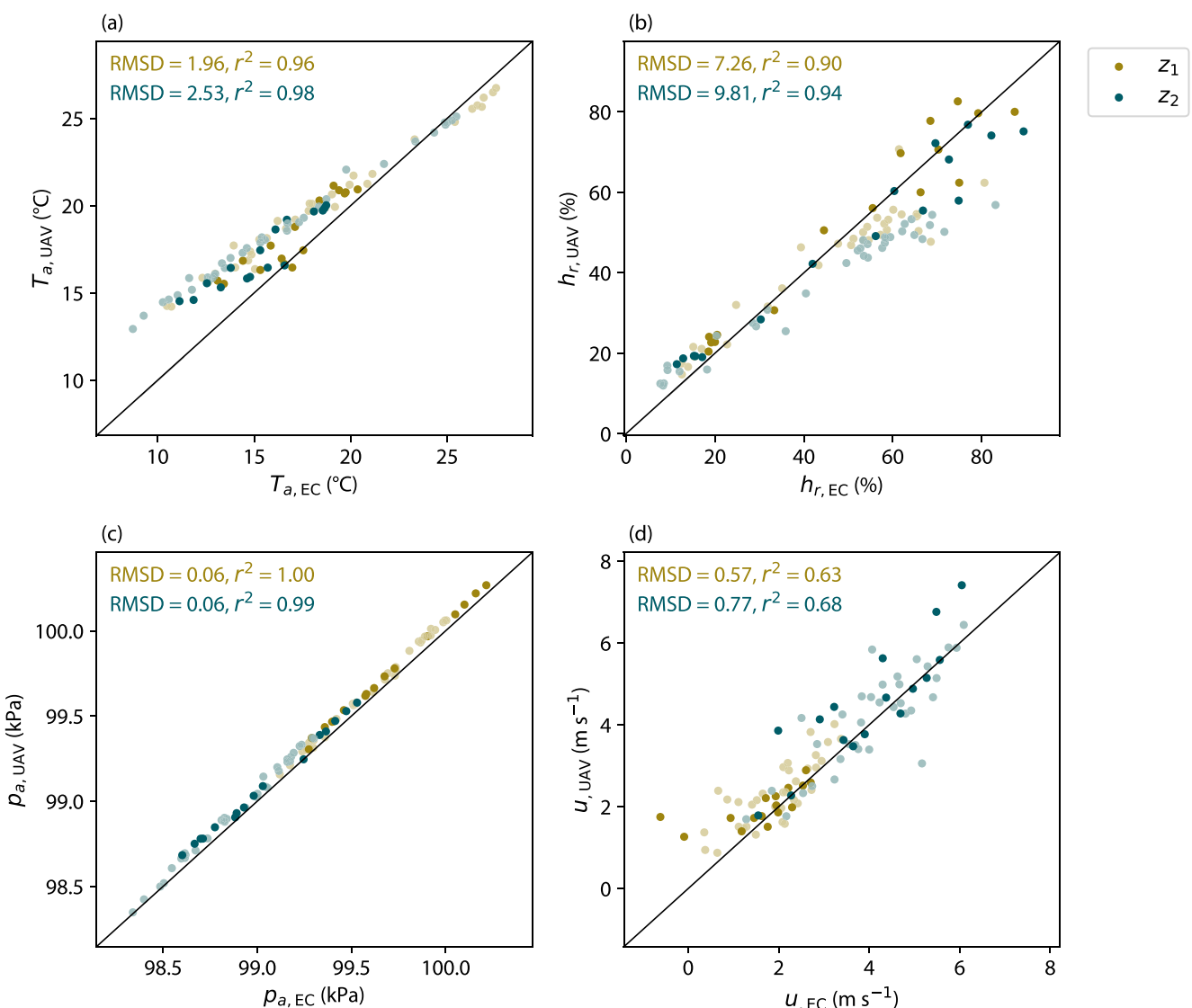


Figure 3. Meteorological parameters. (a) Air temperature, (b) relative humidity, (c) air pressure, and (d) wind speed measured on the unmanned aerial vehicle (“UAV”) compared with tower-derived profile values (“EC”) at the corresponding measurement heights ($z_1 = 1.5$ m, $z_2 = 50.5$ or 60.5 m) for all 50 flights. The darker colors correspond to the 16 Evapotranspiration flights. Data from flights for which tower values were substituted for missing UAV meteorological data (see Table 2) are plotted, but are not included in the summary statistics.

flights. On average, λE from the Dyer and Brutsaert models was within 22.3% and 20.8% of eddy covariance values, respectively, while λE from the Bowen Ratio approach was within 27.3% of λE_{EC} .

4.2.2. Sources of Uncertainty in UAV-Derived λE

In the SEB approach, T_s was by far the main source of uncertainty in UAV-derived λE , contributing 56% of the total $\Delta \lambda E$ on average in the Dyer and Brutsaert models (Figure 7). Corrected T_s from the UAV was 4.9 K higher than the inverted CNR4 temperature, though the footprints were not the same. T_a and r_H were responsible for 20.9% and 7.2% of the total λE uncertainty, respectively, in the Dyer model, and 20.4% and 8.3%, respectively, in the Brutsaert model. In the neutral case, $\partial \lambda E$ due to r_H was higher (18%), as atmospheric conditions were usually unstable during the flights, so modeled r_H without the stability correction functions was too high.

In contrast, T_{a1} and T_{a2} were the main sources of uncertainty in the Bowen Ratio approach, comprising a combined 64.7% of the total uncertainty in λE . Relative humidity measurements also contributed a substantial amount (19.9% combined) of the total uncertainty. Uncertainty due to T_s was much lower than in the SEB approaches, averaging 7.8% of $\Delta \lambda E$ across all flights. Uncertainty due to p_a was negligible (<1%) for all methods.

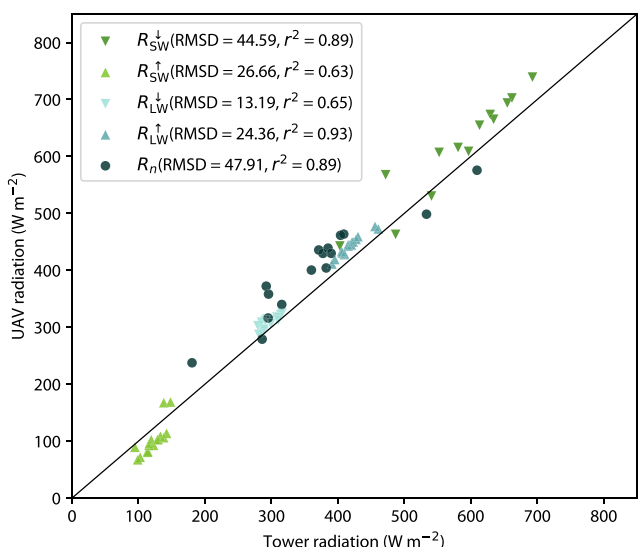


Figure 4. Net radiation and its components from the unmanned aerial vehicle (UAV) compared with measured values from the 4-channel net radiometer net radiometer on the tower. R_{SW}^{\downarrow} was measured on the UAV, and R_{SW}^{\uparrow} , R_{LW}^{\downarrow} , and R_{LW}^{\uparrow} were calculated according to Equations 3–5.

of $\Delta\lambda E$ following the early morning temperature inversion to just 2% at mid-morning. As the magnitude of T_a increases through the rest of the day, so does its control of λE , peaking around 10% in the mid-afternoon, before another spike at dusk when T_{a1} drops below T_{a2} . For all gradients (T_a , h_r , and p_a), values at z_1 and z_2 contribute approximately equally, with slightly greater values at z_1 due to R_{LW}^{\downarrow} . Incoming shortwave radiation (R_{SW}^{\downarrow}) is also much less important for λE in the Bowen Ratio approach than in the SEB approach, consistently contributing 2.6%–4.3% of the total $\Delta\lambda E$ throughout the day.

4.3. Sensitivity of λE in SEB and Bowen Ratio Approaches

Under typical diurnal conditions, λE calculated using the SEB approach is most sensitive to T_s , T_a , and R_{SW}^{\downarrow} (Figure 8a). The change in λE due to ΔT_s is the most important contributor to $\Delta\lambda E$ and remains relatively constant throughout the day, between 32% and 40%. T_a is nearly as important as T_s , accounting for over 40% of $\Delta\lambda E$ in the early morning and evening, and decreasing to 24.1% at midday. The slight decrease in dependence on temperature terms reflects the increasing contributions of R_{SW}^{\downarrow} and r_H , which are minimal at dusk and dawn and rise to 26.5% and 8.3% of $\Delta\lambda E$, respectively, around midday. λE is slightly sensitive to h_r in the early morning and evening (5%–7%), but varies relatively little compared to influence of the other variables (<2%) during the daytime.

By contrast, in the Bowen Ratio approach, the humidity gradient is the largest determinant of $\Delta\lambda E$, accounting for up to 40% of the total $\Delta\lambda E$ during the daytime, with fairly little variation (Figure 8c). Air pressure can be nearly as important, with p_{a1} and p_{a2} comprising up to 38.7% of $\Delta\lambda E$ during the day due to the role of p_a in the potential temperature gradient. Compared to λE_{SEB} , λE_{BR} is much less sensitive to fluctuations in T_s , which accounts for just 11.1% of $\Delta\lambda E$ at midday. $\partial\lambda E_{BR}$ due to T_s shows more diurnal variation, however, reaching as high as 20.5%–33.2% of total $\Delta\lambda E$ in the morning and late afternoon, and briefly up to 78.5% just before 8:00 due to the rise of the inversion layer. Similarly, the role of T_a decreases from a combined 15.3%

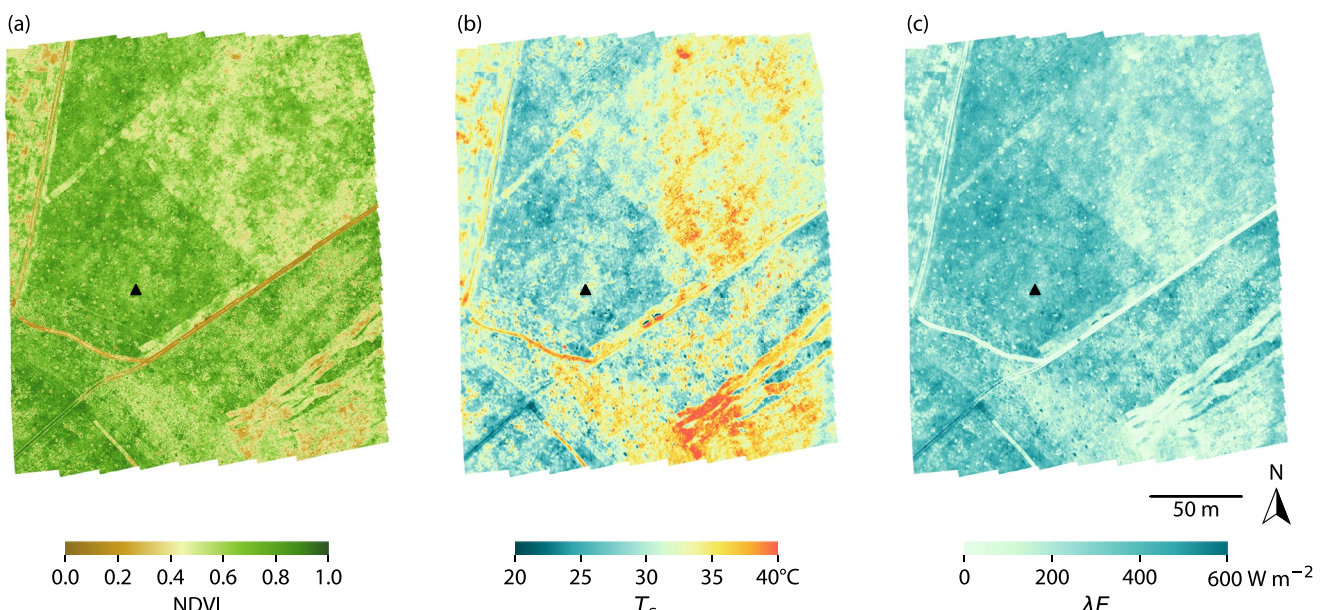


Figure 5. Maps of (a) normalized difference vegetation index, (b) T_s , and (c) λE , calculated using the surface energy balance approach with the Brutsaert resistance formulation, for the 24 March 2021 flight. The black triangle denotes the location of the eddy covariance tower (34.52548°N, 120.41542°E).

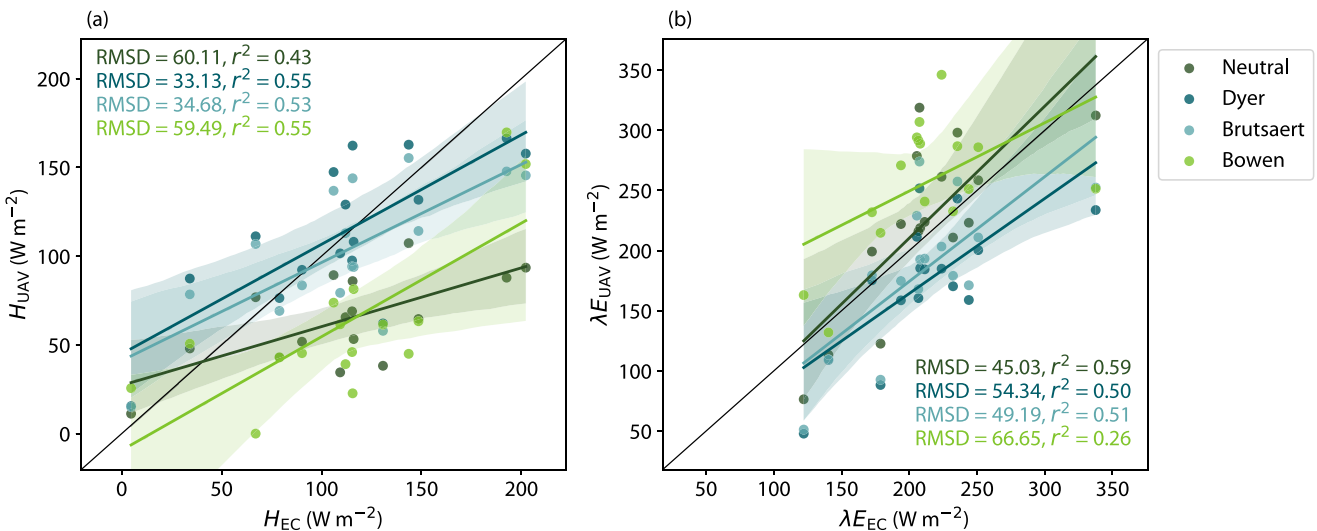


Figure 6. Turbulent fluxes of (a) sensible (H) and (b) latent (λE) heat derived from the unmanned aerial vehicle (“UAV”) using the surface energy balance (Neutral, Dyer, Brutsaert) and Bowen Ratio (Bowen) approaches compared with eddy covariance estimates (“EC”). Linear regression lines are shown for each of the four methods; the shaded regions denote the 95% confidence interval of the regression estimates. For latent heat, λE_{EC} includes the energy balance residual, which was 43.25 W m^{-2} on average during the flights.

4.4. Sources of Uncertainty in λE in SEB and Bowen Ratio Approaches

In addition to evaluating the sensitivity of λE in each approach, we also used the typical measurement uncertainty in each variable (Table 1) to compare the relative contributions to the total λE uncertainty over the course of the day (Figures 8c and 8d). The distinction between these two cases is most obviously demonstrated by R_{SW}^\downarrow , to which λE_{SEB} is very sensitive, but tends to be measured fairly accurately. As a result, given a typical measurement uncertainty of 3%, R_{SW}^\downarrow accounts for <7% of $\Delta \lambda E$ at its maximum in the SEB approach. In contrast, T_s remains the most important variable, comprising between 56.1% and 69.3% of the total uncertainty in λE given a typical measurement uncertainty of $\pm 5 \text{ K}$. Air temperature (T_a) also maintains a similar fraction of $\Delta \lambda E$ as in the previous case, consistently accounting for ~25% of the total uncertainty throughout the

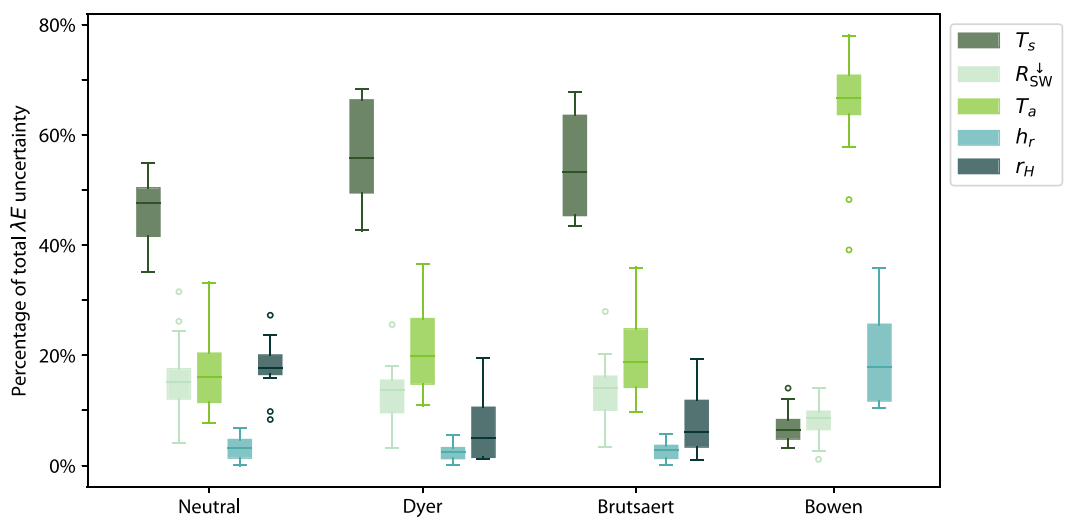


Figure 7. Sources of uncertainty in λE estimates from the unmanned aerial vehicle (UAV) flights. The box plots show the distribution of the fraction of uncertainty in λE due to each variable ($\frac{\partial \lambda E}{\partial x} \frac{\Delta x}{\Delta \lambda E}$) for the three surface energy balance approaches (Neutral, Dyer, Brutsaert) and the Bowen Ratio approach (Bowen). For the Bowen Ratio approach, T_a and h_r are the combined uncertainties at the two measurement heights. Uncertainty due to air pressure was negligible (<1%) for all methods and is not shown. Flights where meteorological data from the tower were substituted for missing UAV data were omitted.

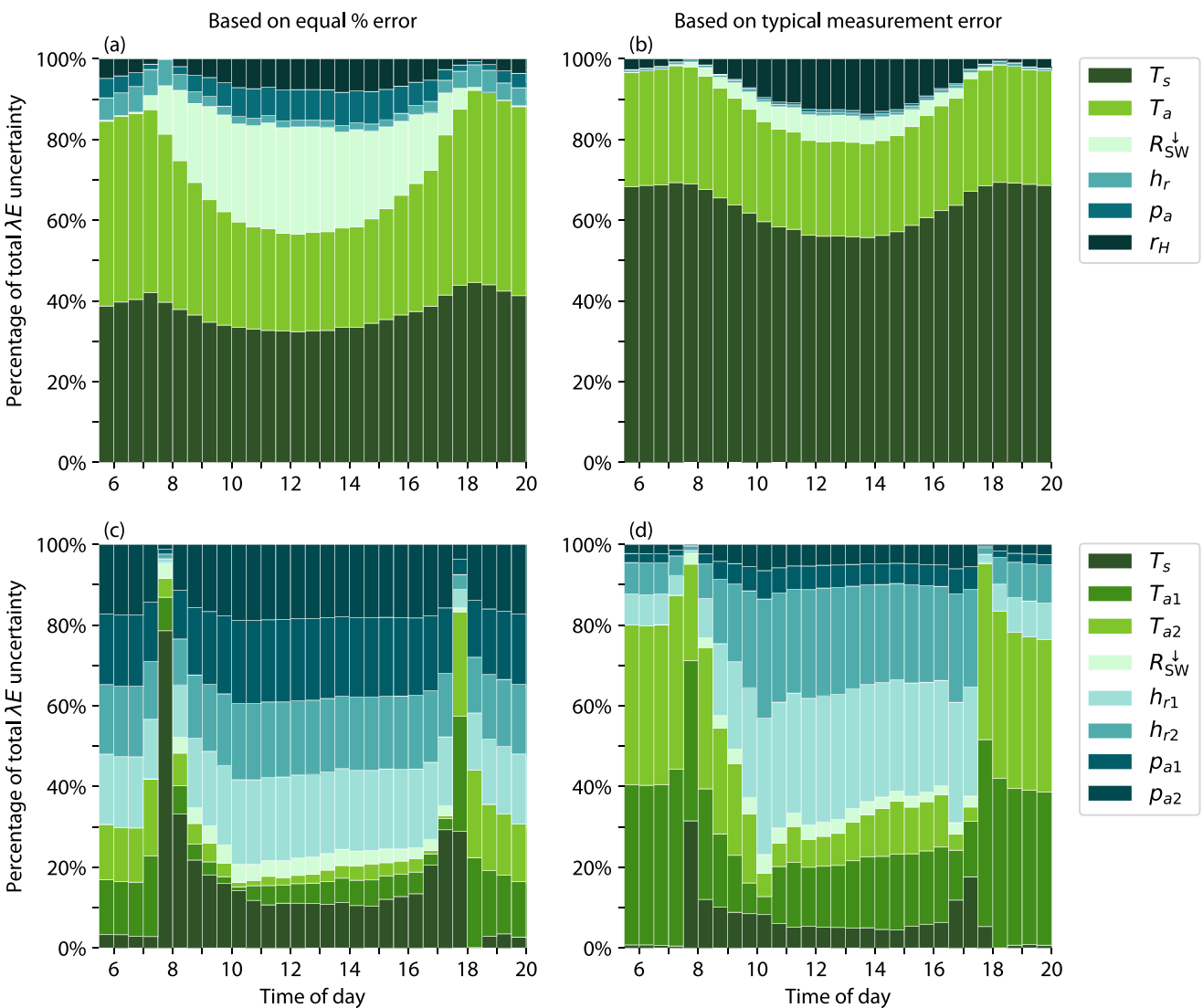


Figure 8. Sensitivity and uncertainty of λE to input parameters. The left column shows the relative sensitivity of λE in the (a) surface energy balance (SEB) (λE_{SEB}) and (c) Bowen Ratio (λE_{BR}) approaches; that is, $\frac{\partial \lambda E}{\partial x} \frac{\Delta x}{\Delta \lambda E}$ given the same $\frac{\Delta x}{x}$ for all variables x . The right column shows the contribution of each variable to the total uncertainty in λE in the (b) SEB and (d) Bowen Ratio approaches given the typical measurement uncertainty (shown in Table 1) in each variable. Uncertainty in λE due to p_a is negligible in the SEB approach.

daytime. Notably, r_H follows an opposite trend to T_s , with a minimal role in the morning and evening periods, but increasing to 13.8% in the middle of the day. Uncertainty in λE due to p_a is negligible (<1%) in the SEB approach.

While h_r contributes <1% of the total uncertainty in λE in the SEB approach, it can account for as much as 63.3% of the total uncertainty in the Bowen Ratio approach, despite its low relative measurement uncertainty of $\pm 3\%$. Air pressure, on the other hand, accounts for a much lower fraction of $\Delta \lambda E$ than in Figure 8c, though it still accounts for 10.0%–13.5% of the total uncertainty throughout the day. Notably, T_a accounts for a substantial portion of $\Delta \lambda E$, as high as 86.9% in the early morning. Between the rise of the thermal inversion layer and a mid-morning humidity inversion, $\partial \lambda E_{\text{BR}}$ due to T_a decreases to just under 10.4%, before increasing again to >30% in the heat of the mid-afternoon. Uncertainty due to T_s is much lower than in the SEB approach, accounting for around 10% of the total $\Delta \lambda E_{\text{BR}}$ in the morning and late afternoon and 4.5%–6.3% between 11:00 and 16:00.

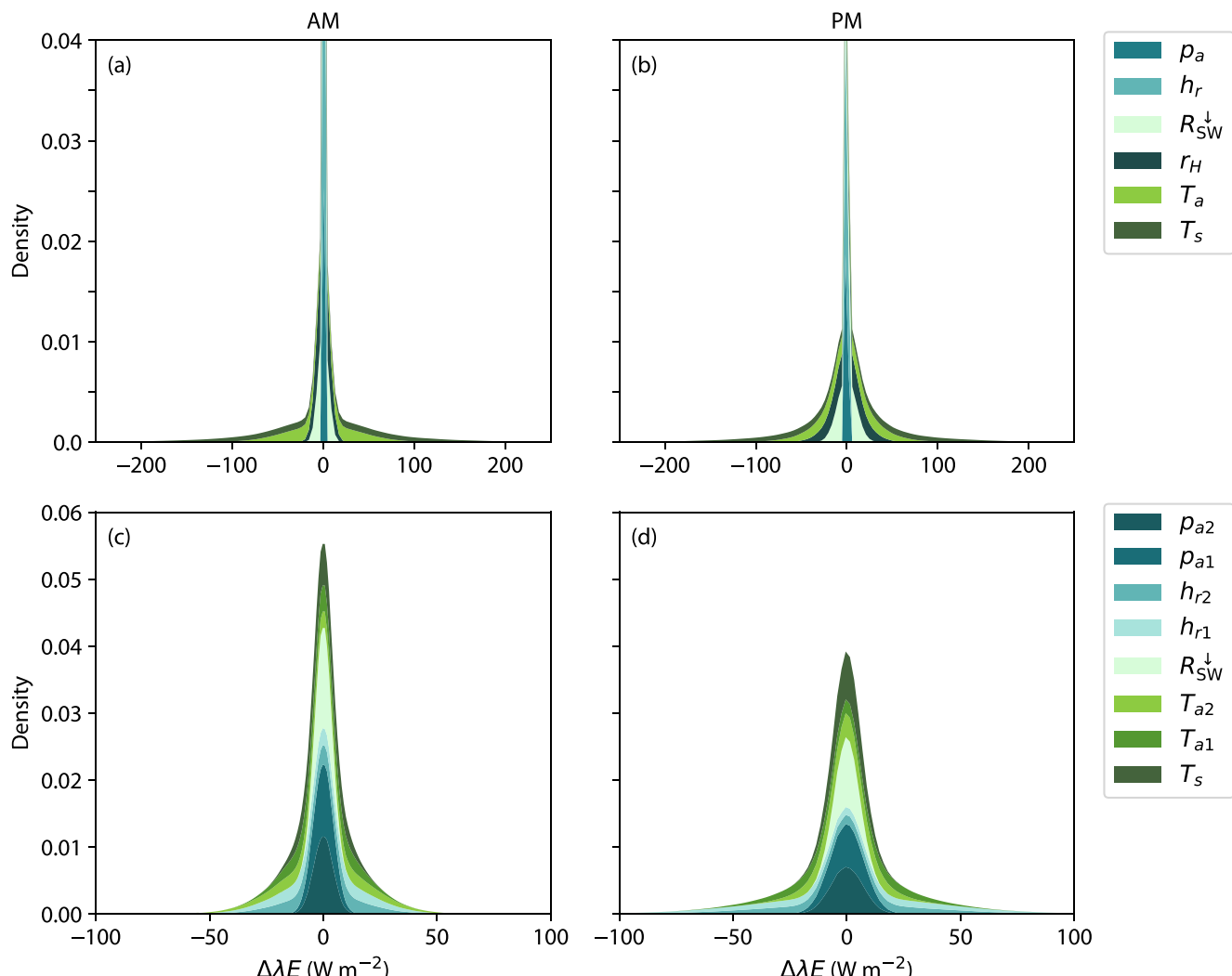


Figure 9. Stacked distributions showing the range of potential absolute uncertainty in λE given typical measurement uncertainties in T_s , R_{SW}^{\downarrow} , T_a , r_H , h_r , and p_a . The top row shows $\Delta\lambda E_{SEB}$ under typical (a) morning (a.m.) and (b) afternoon (p.m.) conditions, and the bottom row shows $\Delta\lambda E_{BR}$ in the (c) morning and (d) afternoon. Note that the range of $\Delta\lambda E$ values differs between the top and bottom rows.

4.5. Potential Uncertainty in λE

Figure 9 shows the distribution of potential uncertainty in λE from the SEB and Bowen Ratio approaches under typical morning (9:30) and afternoon (13:30) conditions. In the SEB approach, the magnitude of potential uncertainty in λE due to R_{SW}^{\downarrow} and r_H increases from morning to afternoon due to the increase in magnitude of these terms. While an estimated typical relative uncertainty of $\pm 20\%$ in r_H leads to a $\pm 11.2 W m^{-2}$ uncertainty in λE in the morning, this potential error increases to $\pm 38.7 W m^{-2}$ in the afternoon. $\Delta\lambda E$ due to uncertainty in T_a , on the other hand, fluctuates very little throughout the day from ± 72.3 to $\pm 79.7 W m^{-2}$. Absolute uncertainty due to T_s is also fairly consistent diurnally, though its magnitude can be as high as ± 171.6 – $191.6 W m^{-2}$. Surface temperature is the only variable that has an inverse relationship with λE (i.e., an overestimate of T_s leads to an underestimation of λE), and its potential absolute uncertainty is greater than that of all other terms combined, though in the opposite direction. Overall, however, while the relative contributions of each source of error change throughout the day, there is little variation in total potential λE uncertainty between the morning and afternoon.

In the Bowen Ratio approach, the range of $\partial\lambda E$ increases slightly for all terms from morning to afternoon. The exception is $\partial\lambda E$ due to T_s , which remains fairly consistent (± 13.7 – $15.7 W m^{-2}$) throughout the day. The potential

total uncertainty in λE increases slightly from morning to afternoon, though the overall magnitude of $\Delta\lambda E_{\text{BR}}$ is consistently much lower than $\Delta\lambda E_{\text{SEB}}$ throughout the day.

5. Discussion

We have presented two novel approaches for quantifying fine-scale transpiration solely from UAV-acquired data. Requiring no ground-based measurements or external inputs, our results are the first independent retrievals of λE from remotely sensed thermal imagery. Of the two approaches, the SEB approach outperformed the Bowen Ratio approach compared to the eddy covariance-derived turbulent fluxes. With resistance formulations that accounted for atmospheric stability, the SEB approach generated independent estimates of λE within ~20% of eddy covariance values, which is within the typical 20%–30% measurement uncertainty of the eddy covariance technique (Allen et al., 2011; Glenn et al., 2007) and consistent with other remote sensing studies. Estimates of λE from satellite data are typically within 15%–30% of ground-based flux measurements with an RMSD of ~50 W m⁻² (Kalma et al., 2008). UAV-based studies have reported RMSD values between 10% and 30% of measured fluxes in irrigated crops (Hoffmann et al., 2016; Kustas et al., 2016; Ortega-Farias et al., 2021), grasslands (Brenner et al., 2018), and savannas (Simpson et al., 2022). Unlike these and other UAV studies, which rely on local flux towers for meteorological input variables, we measured all variables necessary for resolving the SEB equation from the UAV itself. With these independent inputs and a new, fine-scale SEB algorithm, we were able to generate λE values with similar precision as other studies. These results demonstrate how adding characterization of atmospheric properties allows for autonomous, independent observations of λE at very fine scales within the typical range of uncertainty.

The discrepancy between the eddy covariance- and UAV-derived λE values can be partially explained by the difference in available energy ($R_n - G$) between the two sources. UAV-derived R_n was the same for all approaches and was higher than CNR4 measurements for nearly all flights. Interestingly, the main cause of this discrepancy was due to the fact that $R_{\text{SW}}^{\downarrow}$ measured by the LI-200R on the UAV was systematically higher than that of the CNR4, likely due to the difference in the spectral responses of the two pyranometers. The overestimation of shortwave radiation was exacerbated by low albedo values, which led to low $R_{\text{SW}}^{\downarrow}$; surface albedo calculated from the ratio of R_{SW}^{\uparrow} to $R_{\text{SW}}^{\downarrow}$ measured by the tower was ~0.2 during the flight campaigns, on average, while modeled α was ~0.15. While this may be partially due to imperfections in the α model, high NDVI values from the UAV are likely also to blame. Even after radiometric calibration, sensors like the MicaSense Altum can produce imprecise reflectance values due to illumination effects, poor quality calibration panel images, and/or sensor calibration errors (Assmann et al., 2019; Mokhtari et al., 2021); errors in NDVI of ±0.1 can change R_n by up to ±6% (S. Wang et al., 2019). Finally, the average soil heat flux (G) measured at the tower during the flights was 46.8 W m⁻². The modeled G used in the UAV-based estimates was lower than the tower's soil heat flux plates by an average of 8.85 W m⁻², which also increased available energy in the algorithms, propagating to λE . Combined, these effects caused UAV-derived λE to be higher than eddy covariance measurements when H was underestimated.

While comparing λE derived from remotely sensed data to eddy covariance measurements is a common approach for assessing the performance of remote sensing algorithms, it provides just one estimate of accuracy that entirely depends on the accuracy of the eddy covariance data (Glenn et al., 2007). As the energy balance closure problem demonstrates, eddy covariance-derived turbulent fluxes are subject to a number of accuracy issues due to instrument measurement uncertainties, flux corrections, and numerous underlying theoretical assumptions (Foken, 2008; Mauder et al., 2020), leading to relative uncertainties in turbulent fluxes of 20%–30% (Allen et al., 2011; Glenn et al., 2007). Furthermore, λE derived from eddy covariance comprises both transpiration and soil evaporation, while our algorithm focuses solely on calculating transpiration. Though we designed this study to compare the two sources at a time and in a place where evaporation is minimal and transpiration likely makes up the majority of total ET, this distinction also contributes to the discrepancy between tower and UAV-derived fluxes and could explain why UAV-based estimates of transpiration-driven λE are lower than tower values in many cases. In addition, the UAV flights covered over 86% of the tower footprints on average. Given the relative homogeneity of the grassland, the cumulative means of λE_{UAV} from 10% to 90% of the tower fetch area were fairly constant, so the fetch area not covered by a flight would be unlikely to measurably change the estimates. Depending on the composition and size of this area, however, the tower values could differ from the UAV-based estimates more substantially due to their slightly different footprints. Lastly, although we

accounted for the variation in the tower's fetch area and the spatial distribution of the footprint, the mismatch in spatial scale between the tower and UAV-based estimates could also cause the two to differ. Thus, our results, like those of other remote sensing studies at eddy covariance sites, should be viewed as a comparison between two observations, rather than a validation of remote sensing approaches. For this reason, we also developed an analytical method for estimating uncertainty in our approaches that is independent of other measurements of ET or λE .

Using this method, we found that T_s , r_H , and T_a are the main sources of uncertainty in λE derived from the SEB approach (Figures 7 and 8), which is consistent with other SEB algorithms. Though few comprehensive assessments of λE uncertainty have been performed, two of the most widely attributed sources of uncertainty in SEB algorithms are r_{aH} and T_s . Aerodynamic resistance (r_{aH}) is often blamed for λE discrepancies (Glenn et al., 2007; Trebs et al., 2021; K. Zhang et al., 2016), as its dependent variables (roughness lengths, stability terms, etc.) are difficult to characterize (Hogstrom, 1996; Kalma et al., 2008; Sun et al., 1999), but the magnitude of its effect on λE is rarely quantified. Here, we find that uncertainty in the total resistance (r_H) of $\pm 20\%$ can lead to changes in λE of up to $\pm 39.3 \text{ W m}^{-2}$, or 12.9% of the total $\Delta \lambda E$, at midday, and even greater in the mid-afternoon. Surface temperature has a much larger effect, which is consistent with other studies of various existing SEB algorithms (Cleugh et al., 2007; García-Santos et al., 2022; Mallick et al., 2018; K. Zhang et al., 2016). In addition to T_s alone, the temperature gradient, $T_s - T_a$, can also be a large source of uncertainty (Kalma et al., 2008; Timmermans et al., 2007), but T_a is rarely examined in isolation. Our findings indicate that T_a accounts for $\sim 23\%-28\%$ of λE uncertainty under typical diurnal conditions (Figures 7 and 8), which highlights the importance of using accurate meteorological parameters in SEB models.

The ability to directly measure atmospheric conditions from UAV platforms opens up opportunities for new approaches that do not depend on unobservable resistance terms. The Bowen Ratio approach introduced in this study capitalizes on vertically distributed measurements of T_a and h_r in order to derive λE directly. Not only does this approach avoid the need to characterize r_H , but it also minimizes the role of T_s . Instead, T_a and h_r are the main sources of uncertainty in the Bowen Ratio approach, together accounting for 84.7% of the total λE uncertainty on average. The consequence, however, is that smaller relative deviations in these terms—like those we observed—can lead to large uncertainties in λE . In this case, the sensor biases in T_a and h_r had a compounding effect; the humidity gradient was overestimated, and the temperature gradient was underestimated, both of which led to a low Bowen Ratio for nearly all flights. Compared to T_s and r_H , however, errors in T_a and h_r are relatively easy to correct by empirically correcting for sensor bias, using more advanced instruments, and/or redesigning the sampling approach. The temperature data in this study were derived from speed of sound and wind speed measurements from the TSM; though these sonic temperature values were corrected for humidity, they still showed a bias compared to the predicted values from the tower's HMP155, which has an accuracy of $\pm 0.2^\circ\text{C}$ at 20°C . Given the importance of T_a in the Bowen Ratio approach, correction for this bias using tower T_a data could substantially improve λE estimates. In general, accurate measurements of T_a and h_r are easier to obtain than measurements of T_s or estimates of r_H . While the sensors used here yielded T_a and h_r measurements that were good enough to produce λE values within an acceptable range of uncertainty using the SEB approach, a higher level of accuracy in T_a and h_r is required for the Bowen Ratio approach. More advanced sensors and improvements in the sampling approach—including longer measurement times at each height or sampling of multiple heights between the surface and flying altitude—would provide a better characterization of the atmospheric profiles, which could improve λE estimates. Future implementations of this approach with consideration of these concerns could substantially improve the overall results.

Though the Bowen Ratio approach was outperformed by the SEB approach with respect to the eddy covariance measurements in this study, it shows promise for improvement over the SEB approach in the future. In addition to reducing the main sources of uncertainty in SEB models, the Bowen Ratio approach has a lower overall potential λE uncertainty. With simple modifications to the system and/or sampling design as described above, the Bowen Ratio approach could provide better estimates of λE than the SEB approach and existing algorithms. This demonstrates the utility of UAVs as a powerful observational platform for providing independent, high-frequency measurements of fine-scale plant water use across large spatial extents, bridging the gap between in situ measurements and satellite-based observations. The ability to observe ecohydrological processes at the spatial and temporal scales at which they occur can provide unique and valuable insights into plant and ecosystem responses to fluctuating hydroclimatic conditions.

6. Conclusions

This study is the first to derive fine-scale measurements of plant water use solely using UAV-acquired data, constituting a new frontier in ecohydrology, both scientifically and methodologically. Our framework integrates characterization of atmospheric properties with very high-resolution thermal imagery, allowing for autonomous, independent observations of λE at the individual-plant scale. We developed and implemented two theoretical approaches for calculating λE , one based on SEB and one based on atmospheric profiling. We showed that these approaches can generate estimates of λE within 20%–30% of eddy covariance measurements, on par with existing remote sensing algorithms. The SEB approach showed a slightly better match with the flux tower measurements than the Bowen Ratio approach across 16 flights at our grassland site, with different sources of uncertainty for each approach.

We also presented an analytical method for calculating the uncertainty in λE derived from each of our algorithms and used it to show how the sources and magnitude of uncertainty vary throughout the day. We found that T_s , T_a , and r_H are the greatest sources of uncertainty in the SEB approach under typical measurement conditions, contributing to around 56%, 25%, and 14% of the total $\Delta \lambda E$ in the middle of the day, respectively. In the Bowen Ratio approach, however, h_r and T_a contribute the most uncertainty, together accounting for over 90% of the total $\Delta \lambda E$ in the mid-afternoon. Importantly, h_r and T_a are easier to constrain than T_s and the aerodynamic terms, which are notoriously problematic in SEB approaches. As a result, with improvements to the temperature and humidity sensors and/or adjustments in the sampling design, the Bowen Ratio, which minimizes the role of T_s and r_H , has the potential to decrease uncertainty in λE estimates derived from remotely sensed data.

Leveraging advances in sensor technology and novel data processing algorithms to overcome the observational and modeling challenges of existing approaches, this work provides a powerful toolkit for environmental monitoring and understanding of ecohydrological processes in both natural and managed landscapes where traditional approaches are not suitable, such as heterogeneous savannas and riparian corridors. In addition to providing high spatial resolution surface temperature information, UAVs provide the opportunity to obtain direct measurements of the near-surface atmosphere. Not only does this allow for calculation of plant water use independently of external measurements, but it also opens up new possibilities for observing the conditions under which plants are experiencing stress and how they respond to changes in air temperature, atmospheric moisture demand, water availability, and other constraints. A major strength of the approaches presented here for calculating plant water use and estimating associated uncertainty is that they are self-contained and transferable, enabling fine-scale observations of ecosystems anywhere in the world, including those where flux measurements are otherwise difficult to obtain or where larger-scale estimates tend to be biased or incorrect. Such observations at the individual-plant scale are crucial for improving understanding of the fundamental exchange processes between vegetation and the atmosphere and the impacts of climate change on terrestrial ecosystems.

Data Availability Statement

The meteorological data and derived fluxes from the UAV are available with sample code at <https://github.com/brynmorgan/uavet-wrr>. The eddy covariance data are available at <https://doi.org/10.5063/F1QN6570> under a Creative Commons Attribution 4.0 International License (Morgan, 2023a). The UAV orthoimages are available at <https://doi.org/10.5063/F1FB51DM> under a Creative Commons Attribution 4.0 International License (Morgan, 2023b).

Software developed and used in this study include code for processing UAV flight data (flight logs, meteorological data, images, and GNSS logs), flux tower processing and footprint calculations, and code for the ET algorithms (SEB and Bowen Ratio) and uncertainty analysis. The flux tower code is available from Morgan (2023c) and on GitHub. The ET algorithms and uncertainty analysis software are available as a Python package, aeroet 0.1.0 (Morgan, 2023d).

Acknowledgments

This research was supported by a grant from the Zegar Family Foundation (SB200109). BEM's work was supported by an Environmental Solutions Research Accelerator Award from the Schmidt Family Foundation.

References

- Allen, R. G., Pereira, L. S., Howell, T. A., & Jensen, M. E. (2011). Evapotranspiration information reporting: I. Factors governing measurement accuracy. *Agricultural Water Management*, 98(6), 899–920. <https://doi.org/10.1016/j.agwat.2010.12.015>
- Allen, R. G., Tasumi, M., & Trezza, R. (2007). Satellite-based energy balance for mapping evapotranspiration with internalized calibration (METRIC)—Model. *Journal of Irrigation and Drainage Engineering*, 133(4), 380–394. [https://doi.org/10.1061/\(ASCE\)0733-9437\(2007\)133:4\(380\)](https://doi.org/10.1061/(ASCE)0733-9437(2007)133:4(380))

- Anderegg, W. R. (2015). Spatial and temporal variation in plant hydraulic traits and their relevance for climate change impacts on vegetation. *New Phytologist*, 205(3), 1008–1014. <https://doi.org/10.1111/nph.12907>
- Anderegg, W. R., Konings, A. G., Trugman, A. T., Yu, K., Bowling, D. R., Gabbitas, R., et al. (2018). Hydraulic diversity of forests regulates ecosystem resilience during drought. *Nature*, 561(7724), 538–541. <https://doi.org/10.1038/s41586-018-0539-7>
- Assmann, J. J., Kerby, J. T., Cunliffe, A. M., & Myers-Smith, I. H. (2019). Vegetation monitoring using multispectral sensors — Best practices and lessons learned from high latitudes. *Journal of Unmanned Vehicle Systems*, 7(1), 54–75. <https://doi.org/10.1139/juvs-2018-0018>
- Aubinet, M., Vesala, T., & Papale, D. (2012). *Eddy covariance: A practical guide to measurement and data analysis*. Springer Science & Business Media. <https://doi.org/10.1002/978111914236.ch13>
- Aubrecht, D. M., Helliker, B. R., Goulden, M. L., Roberts, D. A., Still, C. J., & Richardson, A. D. (2016). Continuous, long-term, high-frequency thermal imaging of vegetation: Uncertainties and recommended best practices. *Agricultural and Forest Meteorology*, 228–229, 315–326. <https://doi.org/10.1016/j.agrformet.2016.07.017>
- Barbieri, L., Kral, S. T., Bailey, S. C., Frazier, A. E., Jacob, J. D., Reuder, J., et al. (2019). Intercomparison of small unmanned aircraft system (sUAS) measurements for atmospheric science during the LAPSE-RATE campaign. *Sensors (Switzerland)*, 19(9), 2179. <https://doi.org/10.3390/s19092179>
- Bassiouni, M., & Vico, G. (2021). Parsimony vs predictive and functional performance of three stomatal optimization principles in a big-leaf framework. *New Phytologist*, 231(2), 586–600. <https://doi.org/10.1111/nph.17392>
- Bastiaanssen, W. G. M., Menenti, M., Feddes, R. A., & Holtslag, A. A. M. (1998). A remote sensing surface energy balance algorithm for land (SEBAL). I. Formulation. *Journal of Hydrology*, 212(213), 198–212. [https://doi.org/10.1016/S0022-1694\(98\)00253-4](https://doi.org/10.1016/S0022-1694(98)00253-4)
- Bastiaanssen, W. G. M., Pelgrum, H., Wang, J., Ma, Y., Moreno, J. F., Roerink, G. J., & Van der Wal, T. (1998). A remote sensing surface energy balance algorithm for land (SEBAL). Part 2: Validation. *Journal of Hydrology*, 212, 213–229. [https://doi.org/10.1016/s0022-1694\(98\)00254-6](https://doi.org/10.1016/s0022-1694(98)00254-6)
- Berni, J. A., Zarco-Tejada, P. J., Suárez, L., & Fereres, E. (2009). Thermal and narrowband multispectral remote sensing for vegetation monitoring from an unmanned aerial vehicle. *IEEE Transactions on Geoscience and Remote Sensing*, 47(3), 722–738. <https://doi.org/10.1109/TGRS.2008.2010457>
- Beven, K. (1979). A sensitivity analysis of the Penman-Monteith actual evapotranspiration estimates. *Journal of Hydrology*, 44(3), 169–190. [https://doi.org/10.1016/0022-1694\(79\)90130-6](https://doi.org/10.1016/0022-1694(79)90130-6)
- Bonan, G. B. (2016). *Ecological climatology: Concepts and applications*. Cambridge University Press.
- Brenner, C., Thiem, C. E., Wizemann, H. D., Bernhardt, M., & Schulz, K. (2017). Estimating spatially distributed turbulent heat fluxes from high-resolution thermal imagery acquired with a UAV system. *International Journal of Remote Sensing*, 38(8–10), 3003–3026. <https://doi.org/10.1080/01433116.2017.1280202>
- Brenner, C., Zeeman, M., Bernhardt, M., & Schulz, K. (2018). Estimation of evapotranspiration of temperate grassland based on high-resolution thermal and visible range imagery from unmanned aerial systems. *International Journal of Remote Sensing*, 39(15–16), 5141–5174. <https://doi.org/10.1080/01433116.2018.1471550>
- Brutsaert, W. (1982). *Evaporation into the atmosphere: Theory, history, and applications* (Vol. 1). Springer Netherlands. <https://doi.org/10.1007/978-94-017-1497-6>
- Brutsaert, W. (1975). On a derivable formula for long-wave radiation from clear skies. *Water Resources Research*, 11(5), 742–744. <https://doi.org/10.1029/WR011i005p00742>
- Brutsaert, W. (1992). Stability correction functions for the mean wind speed and temperature in the unstable surface layer. *Geophysical Research Letters*, 19(5), 469–472. <https://doi.org/10.1029/92GL00084>
- Brutsaert, W. (1999). Aspects of bulk atmospheric boundary layer similarity under free-convective conditions. *Reviews of Geophysics*, 37(4), 439–451. <https://doi.org/10.1029/1999rg900013>
- Brutsaert, W. (2005). *Hydrology*. Cambridge University Press. <https://doi.org/10.1017/CBO9780511808470>
- Buck, A. L. (1981). New equations for computing vapor pressure and enhancement factor. *Journal of Applied Meteorology and Climatology*, 20(12), 1527–1532. [https://doi.org/10.1175/1520-0450\(1981\)020%3C1527:NEFCVP%3E2.0.CO;2](https://doi.org/10.1175/1520-0450(1981)020%3C1527:NEFCVP%3E2.0.CO;2)
- Butterfield, H. S., Reynolds, M., Gleason, M. G., Merrifield, M., Cohen, B. S., Heady, W. N., et al. (2019). *Jack and Laura Dangermond preserve integrated resources management plan* (Tech. Rep.). The Nature Conservancy.
- Chen, J. M., & Liu, J. (2020). Evolution of evapotranspiration models using thermal and shortwave remote sensing data. *Remote Sensing of Environment*, 237(December 2019), 111594. <https://doi.org/10.1016/j.rse.2019.111594>
- Cheng, Y., & Brutsaert, W. (2005). Flux-profile relationships for wind speed and temperature in the stable atmospheric boundary layer. *Boundary-Layer Meteorology*, 114(3), 519–538. <https://doi.org/10.1007/s10546-004-1425-4>
- Cleugh, H. A., Leuning, R., Mu, Q., & Running, S. W. (2007). Regional evaporation estimates from flux tower and MODIS satellite data. *Remote Sensing of Environment*, 106(3), 285–304. <https://doi.org/10.1016/j.rse.2006.07.007>
- Dyer, A. J. (1974). A review of flux-profile relationships. *Boundary-Layer Meteorology*, 7(3), 363–372. <https://doi.org/10.1007/BF00240838>
- Dyer, A. J., & Hicks, B. B. (1970). Flux-gradient relationships in the constant flux layer. *Quarterly Journal of the Royal Meteorological Society*, 96(410), 715–721. <https://doi.org/10.1002/qj.49709641012>
- Fisher, J. B., Tu, K. P., & Baldocchi, D. D. (2008). Global estimates of the land-atmosphere water flux based on monthly AVHRR and ISLSCP-II data, validated at 16 FLUXNET sites. *Remote Sensing of Environment*, 112(3), 901–919. <https://doi.org/10.1016/j.rse.2007.06.025>
- Foken, T. (2008). The energy balance closure problem: An overview. *Ecological Applications*, 18(6), 1351–1367. <https://doi.org/10.1890/06-0922.1>
- Gao, W. (1995). Parameterization of subgrid-scale land surface fluxes with emphasis on distributing mean atmospheric forcing and using satellite-derived vegetation index. *Journal of Geophysical Research*, 100(D7), 14305–14317. <https://doi.org/10.1029/95JD01464>
- García-Santos, V., Cuxart, J., Jiménez, M. A., Martínez-Villagra, D., Simó, G., Picos, R., & Caselles, V. (2019). Study of temperature heterogeneities at sub-kilometric scales and influence on surface-atmosphere energy interactions. *IEEE Transactions on Geoscience and Remote Sensing*, 57(2), 640–654. <https://doi.org/10.1109/TGRS.2018.2859182>
- García-Santos, V., Sánchez, J. M., & Cuxart, J. (2022). Evapotranspiration acquired with remote sensing thermal-based algorithms: A state-of-the-art review. *Remote Sensing*, 14(14), 1–36. <https://doi.org/10.3390/rs14143440>
- Glenn, E. P., Huete, A. R., Nagler, P. L., Hirschboeck, K. K., & Brown, P. (2007). Integrating remote sensing and ground methods to estimate evapotranspiration. *Critical Reviews in Plant Sciences*, 26(3), 139–168. <https://doi.org/10.1080/07352680701402503>
- Good, S. P., Noon, D., & Bowen, G. (2015). Hydrologic connectivity constrains partitioning of global terrestrial water fluxes. *Science*, 349(6244), 175–177. <https://doi.org/10.1126/science.aaa5931>
- Grace, J. (1981). Some effects of wind on plants. In *Plants and their atmospheric environment* (pp. 31–56). Blackwell Scientific.
- Green, J. K., Seneviratne, S. I., Berg, A. M., Findell, K. L., Hagemann, S., Lawrence, D. M., & Gentile, P. (2019). Large influence of soil moisture on long-term terrestrial carbon uptake. *Nature*, 565(7740), 476–479. <https://doi.org/10.1038/s41586-018-0848-x>

- Heinemann, S., Siegmann, B., Thonfeld, F., Muro, J., Jedmowski, C., Kemna, A., et al. (2020). Land surface temperature retrieval for agricultural areas using a novel UAV platform equipped with a thermal infrared and multispectral sensor. *Remote Sensing*, 12(7), 1075. <https://doi.org/10.3390/rs12071075>
- Hemingway, B. L., Frazier, A. E., Elbing, B. R., & Jacob, J. D. (2017). Vertical sampling scales for atmospheric boundary layer measurements from small unmanned aircraft systems (sUAS). *Atmosphere*, 8(9), 176. <https://doi.org/10.3390/atmos8090176>
- Hoffmann, H., Nieto, H., Jensen, R., Guzinski, R., Zarco-Tejada, P., & Friberg, T. (2016). Estimating evaporation with thermal UAV data and two-source energy balance models. *Hydrology and Earth System Sciences*, 20(2), 697–713. <https://doi.org/10.5194/hess-20-697-2016>
- Hogstrom, U. (1996). Review of some basic characteristics of the atmospheric surface layer. *Boundary-Layer Meteorology*, 78(3–4), 215–246. <https://doi.org/10.1007/BF00120937>
- Jacob, J. D., Chilson, P. B., Houston, A. L., & Smith, S. W. (2018). Considerations for atmospheric measurements with small unmanned aircraft systems. *Atmosphere*, 9(7), 252. <https://doi.org/10.3390/atmos9070252>
- Jiménez, C., Prigent, C., Mueller, B., Seneviratne, S. I., McCabe, M. F., Wood, E. F., et al. (2011). Global intercomparison of 12 land surface heat flux estimates. *Journal of Geophysical Research*, 116(D2), D02102. <https://doi.org/10.1029/2010JD014545>
- Jung, M., Reichstein, M., Margolis, H. A., Cescatti, A., Richardson, A. D., Arain, M. A., et al. (2011). Global patterns of land-atmosphere fluxes of carbon dioxide, latent heat, and sensible heat derived from eddy covariance, satellite, and meteorological observations. *Journal of Geophysical Research*, 116(3), 1–16. <https://doi.org/10.1029/2010JG001566>
- Kalma, J. D., McVicar, T. R., & McCabe, M. F. (2008). Estimating land surface evaporation: A review of methods using remotely sensed surface temperature data. *Surveys in Geophysics*, 29(4–5), 421–469. <https://doi.org/10.1007/s10712-008-9037-z>
- Klijn, N., Calanca, P., Rotach, M. W., & Schmid, H. P. (2015). A simple two-dimensional parameterisation for Flux Footprint Prediction (FFP). *Geoscientific Model Development*, 8(11), 3695–3713. <https://doi.org/10.5194/gmd-8-3695-2015>
- Konings, A. G., Williams, A. P., & Gentile, P. (2017). Sensitivity of grassland productivity to aridity controlled by stomatal and xylem regulation. *Nature Geoscience*, 10(4), 284–288. <https://doi.org/10.1038/geo2903>
- Kustas, W. P., Alfieri, J. G., Nieto, H., Wilson, T. G., Gao, F., & Anderson, M. C. (2019). Utility of the two-source energy balance (TSEB) model in vine and interrow flux partitioning over the growing season. *Irrigation Science*, 37(3), 375–388. <https://doi.org/10.1007/s00271-018-0586-8>
- Kustas, W. P., Nieto, H., Morillas, L., Anderson, M. C., Alfieri, J. G., Hippis, L. E., et al. (2016). Revisiting the paper “Using radiometric surface temperature for surface energy flux estimation in Mediterranean drylands from a two-source perspective”. *Remote Sensing of Environment*, 184, 645–653. <https://doi.org/10.1016/j.rse.2016.07.024>
- Kustas, W. P., & Norman, J. M. (1999). Evaluation of soil and vegetation heat flux predictions using a simple two-source model with radiometric temperatures for partial canopy cover. *Agricultural and Forest Meteorology*, 94(1), 13–29. [https://doi.org/10.1016/S0168-1923\(99\)00005-2](https://doi.org/10.1016/S0168-1923(99)00005-2)
- Mallick, K., Trebs, I., Boegh, E., Giustarini, L., Schlerf, M., Drewry, D. T., et al. (2016). Canopy-scale biophysical controls of transpiration and evaporation in the Amazon Basin. *Hydrology and Earth System Sciences*, 20(10), 4237–4264. <https://doi.org/10.5194/hess-20-4237-2016>
- Mallick, K., Wandera, L., Bhattacharai, N., Hostache, R., Kleniewska, M., & Chormanski, J. (2018). A critical evaluation on the role of aerodynamic and canopy-surface conductance parameterization in SEB and SVAT models for simulating evapotranspiration: A case study in the Upper Biebrza National Park Wetland in Poland. *Water*, 10(12), 1753. <https://doi.org/10.3390/w10121753>
- Marzahn, P., Flade, L., & Sanchez-Azofeifa, A. (2020). Spatial estimation of the latent heat flux in a tropical dry forest by using unmanned aerial vehicles. *Forests*, 11(6), 1–16. <https://doi.org/10.3390/F11060604>
- Matheny, A. M., Bohrer, G., Vogel, C. S., Morin, T. H., He, L., Frasson, R. P. D. M., et al. (2014). Species-specific transpiration responses to intermediate disturbance in a northern hardwood forest. *Journal of Geophysical Research: Biogeosciences*, 119(12), 2292–2311. <https://doi.org/10.1002/2014JG002804>
- Mauder, M., Foken, T., & Cuxart, J. (2020). Surface-energy-balance closure over land: A review. *Boundary-Layer Meteorology*, 177(2), 395–426. <https://doi.org/10.1007/s10546-020-00529-6>
- McCabe, M. F., Rodell, M., Alsdorf, D. E., Miralles, D. G., Uijlenhoet, R., Wagner, W., et al. (2017). The future of Earth observation in hydrology. *Hydrology and Earth System Sciences*, 21(7), 3879–3914. <https://doi.org/10.5194/hess-21-3879-2017>
- McDowell, N., Pockman, W. T., Allen, C. D., Breshears, D. D., Cobb, N., Kolb, T., et al. (2008). Mechanisms of plant survival and mortality during drought: Why do some plants survive while others succumb to drought? *New Phytologist*, 178(4), 719–739. <https://doi.org/10.1111/j.1469-8137.2008.02436.x>
- McNaughton, K. G., & Van Den Hurk, B. J. J. M. (1995). A ‘Lagrangian’ revision of the resistors in the two-layer model for calculating the energy budget of a plant canopy. *Boundary-Layer Meteorology*, 74(3), 261–288. <https://doi.org/10.1007/BF00712121>
- Minkina, W., & Dudzik, S. (2009). *Infrared thermography: Errors and uncertainties*. John Wiley & Sons.
- Minkina, W., & Klecha, D. (2015). Modeling of atmospheric transmission coefficient in infrared for thermovision measurements. In *Sensors and IRS² 2015* (pp. 903–907). <https://doi.org/10.5162/irs2015/1.4>
- Miralles, D. G., Jiménez, C., Jung, M., Michel, D., Ershadi, A., McCabe, M. F., et al. (2016). The WACMOS-ET project – Part 2: Evaluation of global terrestrial evaporation data sets. *Hydrology and Earth System Sciences*, 20(2), 823–842. <https://doi.org/10.5194/hess-20-823-2016>
- Mokhtari, A., Ahmadi, A., Daccache, A., & Drechsler, K. (2021). Actual evapotranspiration from UAV images: A multi-sensor data fusion approach. *Remote Sensing*, 13(12), 2315. <https://doi.org/10.3390/rs13122315>
- Monin, A. S., & Obukhov, A. M. (1954). Basic laws of turbulent mixing in the atmosphere near the ground [In Russian]. *Trudy Geofizicheskij Instituta AN SSSR*, 24(151), 163–187.
- Morgan, B. (2023a). Eddy covariance flux data from Ramajal Field at the Dangermond Preserve, CA, USA, 2021–2022. [Dataset]. Knowledge Network for Biocomplexity. <https://doi.org/10.5063/F1QN6570>
- Morgan, B. (2023b). UAV VSWIR and thermal infrared imagery for a grassland eddy covariance site at the Dangermond Preserve, CA, USA, 2021–2022. [Dataset]. Knowledge Network for Biocomplexity. <https://doi.org/10.5063/F1FB51DM>
- Morgan, B. (2023c). bry nemorgan/ecflux: v1.0.0 (Latest). Zenodo. <https://doi.org/10.5281/zenodo.10067808>
- Morgan, B. (2023d). Aeroet (0.1.0) [Python]. Retrieved from <https://pypi.org/project/aeroet>
- Mu, Q., Heinsch, F. A., Zhao, M., & Running, S. W. (2007). Development of a global evapotranspiration algorithm based on MODIS and global meteorology data. *Remote Sensing of Environment*, 111(4), 519–536. <https://doi.org/10.1016/j.rse.2007.04.015>
- Mueller, B., Hirsch, M., Jimenez, C., Ciais, P., Dirmeyer, P. A., Dolman, A. J., et al. (2013). Benchmark products for land evapotranspiration: LandFlux-EVAL multi-data set synthesis. *Hydrology and Earth System Sciences*, 17(10), 3707–3720. <https://doi.org/10.5194/hess-17-3707-2013>
- Mueller, B., Seneviratne, S. I., Jimenez, C., Corti, T., Hirsch, M., Balsamo, G., et al. (2011). Evaluation of global observations-based evapotranspiration datasets and IPCC AR4 simulations. *Geophysical Research Letters*, 38(6), L06402. <https://doi.org/10.1029/2010GL046230>
- Nieto, H., Kustas, W. P., Torres-Rúa, A., Alfieri, J. G., Gao, F., Anderson, M. C., et al. (2019). Evaluation of TSEB turbulent fluxes using different methods for the retrieval of soil and canopy component temperatures from UAV thermal and multispectral imagery. *Irrigation Science*, 37(3), 389–406. <https://doi.org/10.1007/s00271-018-0585-9>

- Norman, J. M., Kustas, W. P., & Humes, K. S. (1995). Source approach for estimating soil and vegetation energy fluxes in observations of directional radiometric surface temperature. *Agricultural and Forest Meteorology*, 77(3–4), 263–293. [https://doi.org/10.1016/0168-1923\(95\)02265-Y](https://doi.org/10.1016/0168-1923(95)02265-Y)
- Norman, J. M., Kustas, W. P., Prueger, J. H., & Diak, G. R. (2000). Surface flux estimation using radiometric temperature: A dual-temperature-difference method to minimize measurement errors. *Water Resources Research*, 36(8), 2263–2274. <https://doi.org/10.1029/2000WR900033>
- Obukhov, A. M. (1971). Turbulence in an atmosphere with a non-uniform temperature. *Boundary-Layer Meteorology*, 2(1), 7–29. <https://doi.org/10.1007/BF00718085>
- Oki, T., & Kanae, S. (2006). Global hydrological cycles and world water resources. *Science*, 313(5790), 1068–1072. <https://doi.org/10.1126/science.1128845>
- Ortega-Farias, S., Esteban-Condori, W., Riveros-Burgos, C., Fuentes-Peñaillilo, F., & Bardeen, M. (2021). Evaluation of a two-source patch model to estimate vineyard energy balance using high-resolution thermal images acquired by an unmanned aerial vehicle (UAV). *Agricultural and Forest Meteorology*, 304–305(January), 108433. <https://doi.org/10.1016/j.agrformet.2021.108433>
- Park, S., Ryu, D., Fuentes, S., Chung, H., O'Connell, M., & Kim, J. (2021). Mapping very-high-resolution evapotranspiration from unmanned aerial vehicle (UAV) imagery. *ISPRS International Journal of Geo-Information*, 10(4), 211. <https://doi.org/10.3390/ijgi10040211>
- Qiu, G. Y., Yano, T., & Momii, K. (1998). An improved methodology to measure evaporation from bare soil based on comparison of surface temperature with a dry soil surface. *Journal of Hydrology*, 210(1–4), 93–105. [https://doi.org/10.1016/S0022-1694\(98\)00174-7](https://doi.org/10.1016/S0022-1694(98)00174-7)
- Reichstein, M., Bahn, M., Ciais, P., Frank, D., Mahecha, M. D., Seneviratne, S. I., et al. (2013). Climate extremes and the carbon cycle. *Nature*, 500(7462), 287–295. <https://doi.org/10.1038/nature12350>
- Reineman, B. D., Lenain, L., Statom, N. M., & Melville, W. K. (2013). Development and testing of instrumentation for UAV-based flux measurements within terrestrial and marine atmospheric boundary layers. *Journal of Atmospheric and Oceanic Technology*, 30(7), 1295–1319. <https://doi.org/10.1175/JTECH-D-12-00176.1>
- Roman, D. T., Novick, K. A., Brzostek, E. R., Dragoni, D., Rahman, F., & Phillips, R. P. (2015). The role of isohydric and anisohydric species in determining ecosystem-scale response to severe drought. *Oecologia*, 179(3), 641–654. <https://doi.org/10.1007/s00442-015-3380-9>
- Santa Barbara County Flood Control District. (2022). Monthly & yearly rainfall record. Retrieved from <https://www.countyofsfb.org/2322/Monthly-Yearly-Rainfall>
- Santanello, J. A., & Friedl, M. A. (2003). Diurnal covariation in soil heat flux and net radiation. *Journal of Applied Meteorology and Climatology*, 42(6), 851–862. [https://doi.org/10.1175/1520-0450\(2003\)042_0851:DCISHF_2.0.CO;2](https://doi.org/10.1175/1520-0450(2003)042_0851:DCISHF_2.0.CO;2)
- Schlesinger, W. H., & Jasechko, S. (2014). Transpiration in the global water cycle. *Agricultural and Forest Meteorology*, 189–190, 115–117. <https://doi.org/10.1016/j.agrformet.2014.01.011>
- Simpson, J. E., Holman, F. H., Nieto, H., El-Madany, T. S., Migliavacca, M., Martin, M. P., et al. (2022). UAS-based high resolution mapping of evapotranspiration in a Mediterranean tree-grass ecosystem. *Agricultural and Forest Meteorology*, 321, 108981. <https://doi.org/10.1016/j.agrformet.2022.108981>
- Sun, J., Massman, W., & Grantz, D. A. (1999). Aerodynamic variables in the bulk formulation of turbulent fluxes. *Boundary-Layer Meteorology*, 91(1), 109–125. <https://doi.org/10.1023/A:1001838832436>
- Timmermans, W. J., Kustas, W. P., Anderson, M. C., & French, A. N. (2007). An intercomparison of the surface energy balance algorithm for land (SEBAL) and the two-source energy balance (TSEB) modeling schemes. *Remote Sensing of Environment*, 108(4), 369–384. <https://doi.org/10.1016/j.rse.2006.11.028>
- Tran, Q. H., Han, D., Kang, C., Haldar, A., & Huh, J. (2017). Effects of ambient temperature and relative humidity on subsurface defect detection in concrete structures by active thermal imaging. *Sensors*, 17(8), 1718. <https://doi.org/10.3390/s17081718>
- Trebs, I., Mallik, K., Bhattachari, N., Sulis, M., Cleverly, J., Woodgate, W., et al. (2021). The role of aerodynamic resistance in thermal remote sensing-based evapotranspiration models. *Remote Sensing of Environment*, 264, 112602. <https://doi.org/10.1016/j.rse.2021.112602>
- Trugman, A. T., Medvigy, D., Mankin, J. S., & Anderegg, W. R. L. (2018). Soil moisture stress as a major driver of carbon cycle uncertainty. *Geophysical Research Letters*, 45(13), 6495–6503. <https://doi.org/10.1029/2018GL078131>
- Van de Griess, A. A., & Owe, M. (1993). On the relationship between thermal emissivity and the normalized difference vegetation index for natural surfaces. *International Journal of Remote Sensing*, 14(6), 1119–1131. <https://doi.org/10.1080/01431169308904400>
- Vinukollu, R. K., Wood, E. F., Ferguson, C. R., & Fisher, J. B. (2011). Global estimates of evapotranspiration for climate studies using multi-sensor remote sensing data: Evaluation of three process-based approaches. *Remote Sensing of Environment*, 115(3), 801–823. <https://doi.org/10.1016/j.rse.2010.11.006>
- Vivoni, E. R., Rango, A., Anderson, C. A., Pierini, N. A., Schreiner-McGraw, A. P., Saripalli, S., & Laliberte, A. S. (2014). Ecohydrology with unmanned aerial vehicles. *Ecosphere*, 5(10), 1–14. <https://doi.org/10.1890/ES14-00217.1>
- Wang, L., Good, S. P., & Caylor, K. K. (2014). Global synthesis of vegetation control on evapotranspiration partitioning. *Geophysical Research Letters*, 41(19), 6753–6757. <https://doi.org/10.1002/2014GL061439>
- Wang, S., Garcia, M., Bauer-Gottwein, P., Jakobsen, J., Zarco-Tejada, P. J., Bandini, F., et al. (2019). High spatial resolution monitoring land surface energy, water and CO₂ fluxes from an Unmanned Aerial System. *Remote Sensing of Environment*, 229, 14–31. <https://doi.org/10.1016/j.rse.2019.03.040>
- Wang, S., Garcia, M., Ibrom, A., & Bauer-Gottwein, P. (2020). Temporal interpolation of land surface fluxes derived from remote sensing – Results with an unmanned aerial system. *Hydrology and Earth System Sciences*, 24(7), 3643–3661. <https://doi.org/10.5194/hess-24-3643-2020>
- Wei, Z., Yoshimura, K., Wang, L., Miralles, D. G., Jasechko, S., & Lee, X. (2017). Revisiting the contribution of transpiration to global terrestrial evapotranspiration. *Geophysical Research Letters*, 44(6), 2792–2801. <https://doi.org/10.1002/2016GL072235>
- Westoby, M. J., Brasington, J., Glasser, N. F., Hambrey, M. J., & Reynolds, J. M. (2012). ‘Structure-from-Motion’ photogrammetry: A low-cost, effective tool for geoscience applications. *Geomorphology*, 179, 300–314. <https://doi.org/10.1016/j.geomorph.2012.08.021>
- Zhang, K., Kimball, J. S., & Running, S. W. (2016). A review of remote sensing based actual evapotranspiration estimation. *Wiley Interdisciplinary Reviews: Water*, 3(6), 834–853. <https://doi.org/10.1002/wat2.1168>
- Zhang, Z., Tian, F., Hu, H., & Yang, P. (2014). A comparison of methods for determining field evapotranspiration: Photosynthesis system, sap flow, and eddy covariance. *Hydrology and Earth System Sciences*, 18(3), 1053–1072. <https://doi.org/10.5194/hess-18-1053-2014>

References From the Supporting Information

- Campbell, G. S., & Norman, J. (1998). *An introduction to environmental biophysics*. Springer Science & Business Media.
- Jones, H. G., & Vaughan, R. A. (2010). *Remote sensing of vegetation: Principles, techniques, and applications*. OUP Oxford.